The photonic free-electron laser: A numerical study of its fundamental physics

M.W. van Dijk

Master's Thesis
Applied Physics
University of Twente

July 3, 2012

The photonic free-electron laser: A numerical study of its fundamental physics

M.W. van Dijk

Master's Thesis
Applied Physics
University of Twente
July 3, 2012

Graduation committee:
prof. dr. K.-J. Boller
dr. P.J.M. van der Slot
dr. ir. H. Wormeester
dipl.-phys. T. Denis

This work was done at:
Laser Physics and Non Linear Optics (LPNO)
Applied Nanophotonics (ANP)
MESA+ Institute for Nanotechnology
Faculty of Science and Technology
University of Twente
P.O. Box 217
7500 AE Enschede

List of publications

Journal publications

- T. Denis, M. W. van Dijk, J. H. H. Lee, P. J. M. van der Slot and K.-J. Boller, *Single-mode power scaling in a multiple beam photonic free-electron laser*, to be published (2012).
- T. Denis, M. W. van Dijk, J. H. H. Lee, P. J. M. van der Slot, W. L. Vos and K.-J. Boller, *Tunable coherent Cerenkov lasing from photonic crystals*, to be published (2012).
- P. J. M. van der Slot, T. Denis, J. H. H. Lee, M. W. van Dijk and K.-J. Boller, *Photonic free-electron lasers*, IEEE Photon. J., 570 (2012).

Conference Proceedings

- T. Denis, M. W. van Dijk, J. H. H. Lee, P. J. M. van der Slot and K.-J. Boller, *A photonic free-electron laser*, in: Proceedings of CLEO:QELS, (2012).
- J. H. H. Lee, M. W. van Dijk, T. Denis, P. J. M. van der Slot and K.-J. Boller, *Power scalability of a low-gain photonic free-electron laser*, in: Proceedings of IVEC-IVESC, (2012).
- J. H. H. Lee, M. W. van Dijk, T. Denis, P. J. M. van der Slot and K.-J. Boller, *Study of beam focusing techniques for a power- and frequency scalable photonic free-electron laser*, in: Proceedings of IVEC-IVESC, (2012).
- T. Denis, M. W. van Dijk, J. H. H. Lee, P. J. M. van der Slot and K.-J. Boller, *Single-mode power scaling in a multi-beam photonic free-electron laser*, in: Proceedings of IVEC-IVESC, (2012).

Oral presentations

- T. Denis, M. W. van Dijk, J. H. H. Lee, P. J. M. van der Slot and K.-J. Boller, *Fundamental physics of a photonic free-electron laser*, 7th European User Conference, Mannheim, DE (2012).

- J. H. H. Lee, M. W. van Dijk, T. Denis, P. J. M. van der Slot and K.-J. Boller, *Power scalability of a multi-beam photonic free-electron laser*, 7th European User Conference, Mannheim, DE (2012).
- T. Denis, M. W. van Dijk, J. H. H. Lee, P. J. M. van der Slot and K.-J. Boller, *A photonic free-electron laser*, CLEO:QELS, San Jose, USA (2012).
- M. W. van Dijk, T. Denis, J. H. H. Lee, P. J. M. van der Slot and K.-J. Boller, *The photonic free-electron laser: Coherent Cerenkov radiation from photonic crystals*, 24st NNV-symposium on Plasma Physics and Radiation Technology, Lunteren, NL (2012).
- T. Denis, M. W. van Dijk, J. H. H. Lee, P. J. M. van der Slot and K.-J. Boller, *The photonic free-electron laser: Concept, laser dynamics, frequency tuning*, Colloquium of the strategic research orientation: Applied Nanophotonics, Enschede, NL (2011).

Poster presentations

- T. Denis, M. W. van Dijk, J. H. H. Lee, P. J. M. van der Slot and K.-J. Boller, *Single-mode power scaling in a multi-beam photonic free-electron laser*, IVEC-IVESC, Monterey, USA (2012).
- J. H. H. Lee, M. W. van Dijk, T. Denis, P. J. M. van der Slot and K.-J. Boller, *Power scalability of a low-gain photonic free-electron laser*, IVEC-IVESC, Monterey, USA (2012).
- J. H. H. Lee, M. W. van Dijk, T. Denis, P. J. M. van der Slot and K.-J. Boller, *Study of beam focusing techniques for a power- and frequency scalable photonic free-electron laser*, IVEC-IVESC, Monterey, USA (2012).
- T. Denis, M. W. van Dijk, J. H. H. Lee, P. J. M. van der Slot and K.-J. Boller, *Small signal gain calculations for a photonic free-electron laser*, Physics@FOM, Veldhoven, NL (2012).
- T. Denis, M. W. van Dijk, J. H. H. Lee, P. J. M. van der Slot and K. J. Boller, *Pierce gain calculations for a photonic free-electron laser*, Annual Meeting MESA+, Enschede, NL (2011).

Contents

Chapter 1

Introduction

Photonic crystals (PhC) can radically control the propagation and emission of light [1]. This has been utilized to control the emission properties of embedded light sources, such as quantum dots [2–6]. PhC lasers have been set-up using this control to demonstrate unique lasers, showing e.g., ultrafast modulation of spontaneous emission rates and edge emitting quantum cascade lasers [7,8]. However, the wavelength of PhC lasers is still controlled by the embedded emitters as the light emission occurs due to electronic transitions between discrete energy levels of bound electrons [9].

Essentially any wavelength can be emitted by free electrons propagating through a vacuum as continuous electron levels provide the emitting transitions [9]. These so-called free-electron lasers emit coherent radiation when close synchronism between the interacting electromagnetic wave and a plasma wave on the electron beam exists [10,11]. By adjusting the initial velocity of the electron the synchronism shifts to a different wavelength. This wavelength control allows to cover a wide spectral range, ranging from microwaves to X-rays [12]. In traditional FELs this synchronism is achieved by using an alternating static magnetic field of a so-called undulator to convert the kinetic energy of relativistic electrons into coherent radiation. The drawback of undulator based FELs is their extremely large size (facility scale) due to the requirement of relativistic electron energies, e.g., GeV electron beam energies which are used for generation of XUV radiation (LCLS, FLASH).

A compact alternative to undulator-based FELs are slow-wave FELs, which allow for table-top lasers. Only a small electron energy of several keV is required, similar to the cathode ray tubes that were used as televisions [13]. To achieve synchronism between the electromagnetic wave and the electron beam, the phase velocity of the electromagnetic field is reduced by a so-called slow-wave structure. Many different types of structures such as dielectric lined waveguides, gratings or electrical circuits are employed. The resulting lasers are called Cherenkov FEL, Smith-Purcell FEL or microwave tube [14–21].

Each of the aforementioned lasers have very specific properties due to the pattern of the electromagnetic field inside the structure. By controlling the shape of the structure in the aforementioned lasers the gain, frequency and tuning range can be controlled. However, all these devices show a strong decrease in output power as the operating frequency is increased [22–24]. The reason for

this is that the interaction requires sufficiently good beam quality and sufficiently large electron beam current. An increase in operating frequency is associated with a decrease in structure size, and therefore also with a decrease in total current. The beam quality limits the maximum electron density in the beam [23], and therefore the output power drops as it depends on the total beam current. Typically, slow-wave structures supports only a single electron beam.

Multiple electron beams would allow to increase the total beam current to increase the output power. Hence, what would be desired is a slow-wave free-electron laser providing multiple vacuum channels for multiple electron beams. The output power is controlled by the number of electron beams where the wavelength is controlled by the velocity of the electrons and periodicity of the PhC. Also, other properties like gain bandwidth and tuning range can be controlled through PhC design.

A PhC naturally provides many vacuum channels. However, the working principle of coherent Cherenkov emission into photonic crystal modes has not been studied, yet. Only spontaneous Cherenkov emission from a single electron has been described [25]. Recent measurements using a low electron current provided by an electron microscope demonstrated very weak and incoherent emission in the single electron limit [26]. Further, photonic crystals modeled as an effective dielectric medium have been proposed to operate as a slow-wave FEL [27].

In this thesis we numerically study the working principle of a novel photonic crystal laser based on the coherent emission of free electrons, which we call: the photonic free-electron laser (pFEL). In Chapter 2 we summarize the theory of slow-wave FELs and photonic crystals. Next, in Chapter 3 we show how the small-signal theory of slow-wave FELs can be applied to design a photonic crystal for a pFEL. Chapter 4 will focus on the nonlinear dynamics of the pFEL, for the example of a single-beam device. Amongst others, output power and frequency tuning will be investigated. Subsequently, we will expand the single-beam pFEL to a two-beam pFEL. As the noise in both electron beams is uncorrelated, the radiation generated by the two beams will initially be uncorrelated. As the electron beams will influence each other through the combined radiation field, correlation between the beams will be established. This process is studied in Chapter 5. Finally, in Chapter 6 we will summarize the conclusions.

Chapter 2

Theory

When a charged particle is propagating alongside an object, e.g., a small post, the charged particle induces a dipole in that post. As the particle passes along the post the dipole rotates accordingly. Subsequently, when an electric dipole rotates, it emits an electromagnetic wave. If such an effect is repeated with a charged particle propagating alongside a row of posts, the particle induces a dipole in every post and every posts emits a wave. Such an experiment can be done by using multiple charged particle passing along the posts, each separated by a same distance, exactly matching the wavelength of the generated radiation, and propagating with the same velocity. The generated waves would then constructively interfere if the propagating particles have the same velocity as the phase velocity of the generated wave. To decrease the phase velocity of a wave to the velocity of the electron one can use for example so-called slow-wave structures, e.g., photonic crystals.

When the stream of orderly charged particles is replaced by an electron beam where the particles are ordered in a random manner, and numerous electrons are present within one wavelength, the same result of constructively interfering waves can be achieved when bunches are formed in the electron beam. Bunches can form when the electrons co-propagate with a wave possessing a longitudinal electric field component. In the rest frame of the electron beam, part of the electrons which experience an electric field in the backward direction are accelerated. The other part of the electrons which experience an electric field in the forward direction are decelerated. This effect provides a bunching mechanism for the electron beam.

The combination of both effect described above is the basis for the working principle of the pFEL. This chapter will focus in more depth on the theory of such a laser, which is used in the latter chapters to investigate the pFEL in more detail.

2.1 Cherenkov effect

In a vacuum, the speed of a propagating electromagnetic wave is a universal constant, namely the speed of light, c. The speed of light acts as an upper limit of the velocity attainable by objects possessing a mass [28, 29]. When a light wave is propagating inside a material, its phase

velocity is usually reduced to c/n, where $n > 1$ is the index of refraction of the medium [30]. The phase velocity is defined as $2\pi\nu/k$, where ν and k are the frequency and the wave number of the electromagnetic field, respectively. For example, the index of refraction of silica glass at visible light wavelengths is approximately 1.5, meaning that the phase velocity of light inside the glass is $\frac{2}{3}c$.

When a charged particle, e.g., an electron is traveling through a medium, its Coulomb field displaces the bound electrons in atoms around the position of the particle and induce a transient polarization in the atoms. Therefore, as a response to a passing electron the polarized atoms act as an oscillating dipole which leads to the emission of radiation [31]. Two separate cases can be distinguished based on the velocity of the electron. The first case is when the velocity of the electron is lower than the phase velocity of the electromagnetic field. In this case the radiation field emitted by the oscillating dipoles precedes the electron exciting the dipoles. At a distance, no propagating electromagnetic field is observed in this case, as the emitted fields destructively interfere.

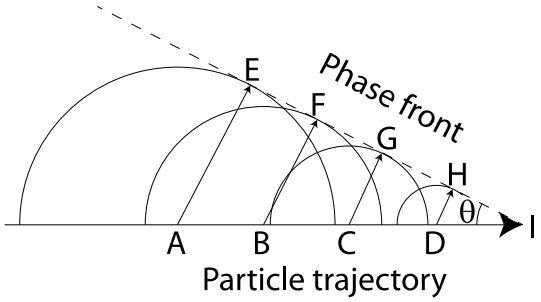

Figure 2.1: *Huygens diagram to illustrate the angle of emission of Cherenkov radiation*

The second case is when the electron is traveling faster than the phase velocity inside the medium, which was first observed by Cherenkov [32] and described subsequently by Frank and Tamm [33]. In this case the radiation field of the electron can not propagate in front of the electron, since the velocity of the electron exceeds the velocity of the radiation field. This means that the electric field around the electron becomes asymmetric. It turns out that a propagating electromagnetic field is generated by the oscillating dipoles, with a phase front under an angle θ with respect to the propagation direction of the electron as shown in Figure 2.1.

In the figure, the electron is moving along the direction of the horizontal arrow with velocity $v_{el} = AI/4\Delta t$, where AI is the distance traveled by the electron in time $4\Delta t$. Along this path, radiation is emitted by dipoles at position A, B, C and D when the electron passes these positions, each a time interval Δt after each other. All dipoles emit radiation which propagates with the phase velocity inside the material, $v_{ph} = c/n$, in all directions with respect to the emitting dipole. In the same time as the electron travels a distance AI in $4\Delta t$, the emitted wave at A travels a distance AE. However, since we consider $v_{el} > v_{ph}$, the phase front emitted by A, B, C and D form a cone around the particle trajectory. From the diagram, the so-called Cherenkov emission angle

can be calculated using

$$\sin(\theta) = \frac{AE}{AI} = \frac{4\Delta t v_{ph}}{4\Delta t v_{el}} = \frac{v_{ph}}{v_{el}} \tag{2.1}$$

Note that no such phase front is formed if the velocity of the particle is too low, $v_{el} < v_{ph}$. Mathematically this corresponds to the angle θ becoming imaginary. The radiation emitted for $v_{el} > v_{ph}$ is named Cherenkov radiation, after its first observer.

When inserting $n = c/v_{ph}$ into Equation 2.1, we see that all materials where the refractive index is larger than unity enable Cherenkov emission. Materials like gases with a refractive index very close to unity need extremely relativistic electrons for Cherenkov emission to occur. In solid or liquid media with higher refractive index a lower electron velocity is sufficient. A typical example where Cherenkov radiation is observed is the blue glow in the cooling water of a nuclear fission reactor [34]. In principle, low or mildly relativistic electrons propagating through bulk material can also produce Cherenkov radiation. However, this process is suppressed by other effects taking place, such as electron scattering or bremsstrahlung.

To avoid these effects and obtain Cherenkov radiation, electrons can be passed very close over the surface of a dielectric material. The Coulomb field of the electron still can polarize the atoms in the material. This effect is utilized in a Cherenkov FEL, which enables interaction with mildly relativistic electrons ($E_{kin,el} > 70$ keV). However, the electric field inside the material decreases as a function of distance from the surface of the dielectric and on the scale of a wavelength, which makes it very difficult to realize Cherenkov lasers with short wavelengths.

To utilize even slower electrons, effective dielectrics such as electrical circuits are applied at microwave frequencies. An other class of effective dielectrics are photonic crystals whose use is studied in this thesis. Photonic crystals are discussed in more detail in Section 2.3.

2.2 Fundamental equations

The effective dielectric medium approach for photonic crystals can successfully explain the emission of radiation due to propagating electrons inside photonic crystals. However, this approach does not take into account the actual spatial shape of the electromagnetic field distribution inside a photonic crystal. As has been discussed in literature, the electromagnetic field distribution and polarization inside photonic crystals is clearly different from that in a homogeneous dielectric and lead, e.g., to an enhanced or suppressed spontaneous emission rate [2, 6].

To describe the actual electromagnetic fields inside a photonic crystal a full field analysis of the pFEL is required. Electromagnetic fields are described by the Maxwell equations [30]

$$\nabla \times \mathbf{H}(\mathbf{r},t) = \mathbf{J}(\mathbf{r},t) + \frac{\partial \mathbf{D}(\mathbf{r},t)}{\partial t}; \tag{2.2}$$

$$\nabla \times \mathbf{E}(\mathbf{r},t) = -\frac{\partial \mathbf{B}(\mathbf{r},t)}{\partial t}; \tag{2.3}$$

$$\nabla \cdot \mathbf{B}(\mathbf{r},t) = 0; \tag{2.4}$$

$$\nabla \cdot \mathbf{D}(\mathbf{r},t) = \rho(\mathbf{r},t). \tag{2.5}$$

Here $\rho(\mathbf{r},t)$ is the space charge density, $\mathbf{J}(\mathbf{r},t)$ the current density, $\mathbf{E}(\mathbf{r},t)$ the electric and $\mathbf{H}(\mathbf{r},t)$ the magnetic field. All quantities can explicitly dependent on the location $\mathbf{r}$ and the time t. Throughout this thesis the electric displacement field $\mathbf{D}(\mathbf{r},t)$ is assumed to be linearly dependent on the electric field

$$\mathbf{D}(\mathbf{r},t) = \varepsilon_0 \varepsilon(\mathbf{r}) \mathbf{E}(\mathbf{r},t), \tag{2.6}$$

where ε_0 is the vacuum permittivity and ε is a scalar describing the dielectric material properties. Note that in a photonic crystal, ε usually depends explicitly on the location $\mathbf{r}$ mostly in a periodic manner. For the magnetic flux density we find generally

$$\mathbf{B}(\mathbf{r},t) = \mu_0 \mu(\mathbf{r}) \mathbf{H}(\mathbf{r},t) \tag{2.7}$$

where μ_0 is the vacuum permeability and μ is describing the magnetic material properties. However, in this thesis we discuss only non-magnetic materials and we set μ to unity.

The Maxwell equations also include the continuity equation:

$$\nabla \mathbf{J}(\mathbf{r},t) + \frac{\partial \rho(\mathbf{r},t)}{\partial t} = 0 \tag{2.8}$$

which expresses that the total electric charge of an isolated system remains constant regardless of temporal or local changes within the system itself.

To describe the interaction of the electrons with the electric and magnetic fields we use the Newton-Lorentz equation:

$$m \frac{\mathrm{d}[\gamma(\mathbf{r},t)\mathbf{v}(\mathbf{r},t)]}{\mathrm{d}t} = q_e \left[\mathbf{E}(\mathbf{r},t) + \mathbf{v}(\mathbf{r},t) \times \mathbf{B}(\mathbf{r},t)\right]. \tag{2.9}$$

Here, m is the electron mass, γ is the relativistic factor, $\mathbf{v}$ is the electron velocity and $q_e = -e$ is the electron charge. By self-consistently analyzing the set of nonlinear differential equations (2.2)–(2.9) one can fully describe the generation of coherent Cerenkov emission inside photonic crystals. These equations form a system of nonlinear, coupled differential equations which is mathematically very complex to solve. A first approach to solve them is to use a linear approximation using coupled mode theory. In this approximation the waves propagating in the photonic crystal are investigated separately from the motion of the electrons (space-charge waves). Note that this approximation is only valid for a sufficiently weak interaction of the electrons with the electromagnetic field, i.e., at low field strengths and low electron densities. In a second step this approximation will be given up for the calculation of strongly interacting electron densities and electromagnetic fields.

2.3 Photonic crystals

Materials in which the dielectric constant varies periodically in space on the order of an optical wavelength are called photonic crystals [35]. Photonic crystals offer an unprecedented control of

the optical properties of light with such wavelengths, such as photonic waveguides.

The simplest model of a photonic crystal would be to describe it as an effective dielectric material. This approach explains the emission of Cerenkov radiation from electrons inside a photonic crystal, but it can not explain the strength of the light emission. For such description the spatial shape (distribution and polarization) of the electromagnetic fields inside the photonic crystals must be included, which is neglected by effective dielectric approaches. The shortcomings of effective dielectric material models are clearly demonstrated by Cerenkov emission of a single electron [25].

Three different classifications of photonic crystals can be distinguished, each relating to the number of spatial dimensions showing translational symmetry [35]. A widely used example of a one-dimensional photonic crystal, assuming that the non-periodic dimensions of the crystal extend into infinity, is a multilayer dielectric mirror, such as a quarter-wave stack. Such a dielectric mirror consists of alternating layers of materials with different dielectric constants. In a similar manner we can define a two-dimensional photonic crystal. In a two-dimensional crystal two out of three spatial dimensions have translational symmetry. Again we assume that the non-periodic dimension extends to infinity. An example of such a two dimensional photonic crystal can be an infinite array of posts of infinite length. A three dimensional photonic crystal would be a crystal with translational symmetry in all three spatial dimensions, such as a cubic crystal or a so-called body-centered cubic, well-know from solid state crystals. Throughout this thesis, only photonic crystals with one-dimensional translational symmetry (here z-direction) are considered. Therefore, all later discussions will be limited to a one-dimensional approach.

For photonic crystals consisting of metals, the Maxwell equations (2.2–2.7) are linear because the current density $\mathbf{J}(\mathbf{r}, t)$ and space-charge density $\rho(\mathbf{r}, t)$ are zero. In this case it has been shown that solving the Maxwell equations is equivalent to an eigenvalue problem [35]. Furthermore, numerous numerical methods exist to solve such eigenvalue problems [36]. Because of the periodic nature of the photonic crystal, numerical calculations can be limited to a single unit cell by applying periodic boundary conditions to the edge of the unit cell. For the one-dimensional photonic crystals considered here, if applying periodic boundary conditions in the z-direction, this implies that the considered structure is infinitely long in the z-direction. Using readily available numerical techniques together with proper boundary conditions, the shape and frequencies of characteristic, orthonormal electric field distributions, i.e., eigenmodes and eigenfrequencies, inside a photonic crystal can be retrieved [35, 37, 38].

The collection of all eigenfrequencies as a function of wave number can be plotted in the form of a band diagram of the photonic crystal, analogous to the band diagram found for electrons in solids [39, 40]. Due to the periodic nature of the photonic crystal, the band diagram is periodic, i.e., it repeats itself every $2\pi m/a_z$, where a_z is the lattice constant along z and m is an integer.

The resulting eigenmodes are also spatially periodic in the direction in which the photonic crystal is periodic [35]. It is well known that all periodic functions can be expressed as an infinite

Fourier series [39]. Expressing the electric field in a photonic crystal yields:

$$E(x,y,z) = \sum_{m=-\infty}^{\infty} E_m(x,y)e^{-ik_z z} \tag{2.10}$$

with

$$k_z = k_0 + 2\pi\frac{m}{a_z}. \tag{2.11}$$

Here, k_0 is the fundamental wave number, i.e., the wave number within the 0^{th} order spatial harmonic, also called the Brillouin zone. Note that each so-called spatial eigenmode has a different phase velocity. For any type of FEL, amplification occurs close to synchronism ($v_{el} = v_{ph}$ with $v_{ph} = 2\pi\nu/k_z$ and ν is the eigenfrequency at wave number k_z) [11]. Hence, the Fourier decomposition of the periodic eigenmode and the field amplitude at the synchronized wave number turns out to be required to calculate the small signal gain of a pFEL, as explained in Section 2.5

2.4 Plasma waves

A collection of neutral particles, mobile ions and unbound electrons is known as a plasma [41]. The long range nature of the electric and magnetic interactions between individual particles can induce collective motions in a plasma called plasma or space-charge density waves. The electron beam of a pFEL is also a plasma and space-charge density waves can propagate on the beam. Space-charge density waves are longitudinal waves with a spatial modulation of the charge density. For example, let us consider a stationary electron beam in the rest frame of the electron beam which is infinitely long, analogous to the explanation used by Gilmour [42]. We assume that stationary positively charged ions cancel out the space charge of the beam. When all electrons are placed equidistantly to each other, all repelling forces cancel out and all electrons stay fixed at their initial position. However, when electrons are displaced by a tiny amount, this stability is disturbed and the Coulomb force pulls the displaced electrons back, acting as a restoring force. Hence, an oscillation around their stationary position results. The frequency of that oscillation is the so-called plasma frequency:

$$\nu_p = \frac{1}{2\pi}\sqrt{\frac{-e\rho}{m_e\varepsilon_0}}, \tag{2.12}$$

which increases with the charge density ρ.

For a moving electron beam with a spatially non-uniform charge density a further effect appears. Even with a charge density so small that electrons effectively do not influence each other, a spatial variation along z in the electron beam is seen by a standing observer as a propagating wave. The dispersion of that wave, i.e., the relation between the spatial and temporal periodicities, is given by the velocity with which the beam passes the observer as $2\pi\nu = v_{el}k$.

Following Gilmours description [42] of a space-charge wave on a moving electron beam, we can derive the wave equation from Maxwell's equations (2.2–2.7) in the presence of space charge and current density. Concentrating on the electric field component in the longitudinal direction this

results in

$$\frac{\partial^2 E_z}{\partial z^2} - \frac{\varepsilon}{c^2}\frac{\partial^2}{\partial t^2}E_z = -\mu_0 \frac{\partial}{\partial t} J_z - \frac{1}{\varepsilon_0}\frac{\partial \rho_z}{\partial z}. \tag{2.13}$$

Even though we limit ourselves to the z-component alone, the current density, $J_z = \rho(z,t)v_{z,e}(z,t)$, still forms a non-linear term in the equations. The standard procedure to find a solution is to linearize all equations. To linearize them J_z is split into a DC and an RF component:

$$\begin{aligned} J_z(z,t) &= J_{z,DC} + J_{z,RF}(z,t) && (2.14)\\ &= (\rho_{DC} + \rho_{RF}(z,t))\,(v_{z,DC} + v_{z,RF}(z,t)) && (2.15)\\ &= \rho_{DC}v_{z,DC} + \rho_{RF}(z,t)v_{z,DC} + \rho_{DC}v_{z,RF}(z,t) + \rho_{RF}(z,t)v_{z,RF}(z,t). && (2.16) \end{aligned}$$

To obtain a linear approximation, the first and last term in Equation 2.16 are neglected. Because we assume an interaction at a certain frequency ($e^{i2\pi\nu t}$) and with a certain wavelength ($e^{ik_z z}$), we rewrite all oscillating terms as:

$$A_z(z,t) = A_{DC} + \tilde{A}_{RF}e^{i(2\pi\nu t - k_z z)}. \tag{2.17}$$

where only the RF term is taken into account.

Using 2.13 and the continuity equation (2.8) an expression describing how the beam current density is related to the oscillating longitudinal electric field can be obtained:

$$\tilde{J}_{z,RF} = i2\pi\nu\epsilon_0 \frac{4\pi^2\nu_p^2}{(2\pi\nu - k_z v_{z,0})^2}\tilde{E}_{z,RF}, \tag{2.18}$$

Alternatively, Equation 2.18 describes how the electric field can be driven by an oscillating beam current density. This is what we are going to use in the small signal gain calculations of the pFEL in the next section.

For the eigenmodes of the space-charge wave two solutions can be found [43], namely

$$k_z = 2\pi\frac{\nu \pm \nu_p}{v_{z,DC}}. \tag{2.19}$$

If we calculate the phase velocity of both solutions,

$$v_{ph} = \frac{v_{z,DC}}{1 \pm \nu_p/\nu}, \tag{2.20}$$

we can distinguish two velocities. One of the solutions has a phase velocity which is slightly higher than the DC velocity of the electron beam. Hence, this solution is called the fast space-charge wave. To excite it, the electrons need to acquire a slightly higher kinetic energy (on average). For the other solution, called the slow space-charge wave, the phase velocity is slightly slower than the DC velocity of the electron beam.

In the pFEL, a radiation field is generated at the expense of the electron beam energy. Initially

the electron beam is injected in the pFEL with only a DC component. When the electrons emit radiation, only the slow space-charge wave can be exited. A growing fast space-charge wave is not possible as it requires an increase in average electron kinetic energy and there is no source for this energy when there is no radiation field, which is the case when we start from noise.

2.5 Small-signal amplification

Pierce's small-signal gain theory is valid for slow-wave vacuum electron devices including e.g., traveling wave tubes and backward-wave oscillators. In the small-signal gain (amplification) regime, i.e., the energy of the beam remains unchanged to first approximation, which means that the application of the coupled mode theory is well justified [42]. In coupled mode theory, the modes of the propagating electromagnetic field in the PhC and the modes of the space-charge waves on the electron beam are calculated separately. It is assumed that an interaction between the modes occurs only when frequency and wave number of the electromagnetic field and the space charge waves are equal. Therefore, we need to calculate how an electron beam induces an electromagnetic field and how the electromagnetic field influences the electron beam. According to Pierce [15], the small signal amplification is given by

$$G = 47.3 \sqrt[3]{\frac{Z_P}{Z_B}} \text{ (dB per wavelength)}, \tag{2.21}$$

where Z_P and Z_B are impedances that summarize the properties of the field distribution for the considered eigenmode and the properties of the electron beam, respectively. The beam impedance is given by the acceleration voltage U and the beam current I,

$$Z_B = 4\frac{U}{I}. \tag{2.22}$$

To take into account the spatial extent of the electron beam, we average over the overlap area of the electric field of the eigenmode and the electron beam. Therefore, the Pierce impedance is defined as

$$Z_P = \frac{\frac{1}{A_b}\int_{A_b} |E_{z,m}(x,y)|^2 \, \mathrm{d}\mathbf{A}}{k_z^2 P_{flux}}; \tag{2.23}$$

$$P_{flux} = \frac{v_g \mathcal{E}_{stored}}{a_z}. \tag{2.24}$$

Here, P_{flux} is the energy propagating through a transverse plane of the photonic crystal within a certain time, a_z is the periodic lattice constant, $\mathcal{E}_{stored}$ is the stored energy in a single unit cell and v_g is the group velocity at the velocity matched (interaction) wave number k_z. The electric field, $|E_{z,n}(x,y)|$ is the magnitude of the z-component of the eigenmode field at the velocity matched wave number calculated by the Fourier decomposition as given in Equation 2.10. Because only the part of the eigenmode field synchronous to the electron beam can exert an effective force over long

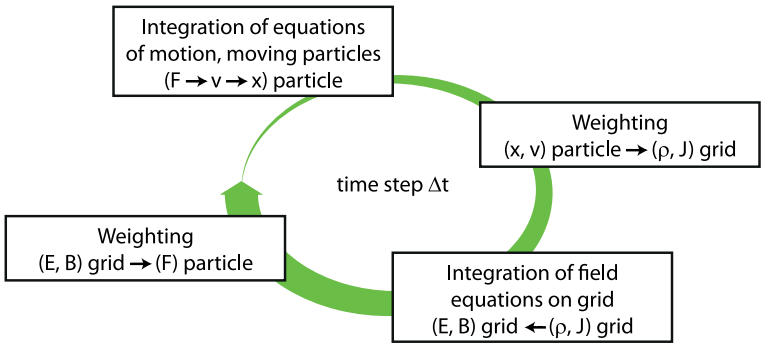

Figure 2.2: *Illustration of a single time cycle for a PIC algorithm.*

distances it is solely responsible for bunching.

2.6 Particle-in-cell method

To be able to take nonlinear effects into account, i.e., the full mutual interaction of the electron beam and the electromagnetic field inside the PhC, we need to solve Maxwell's equations (2.2–2.7) and the Newton-Lorentz equation 2.9 for each electron self consistently. A particle-in-cell (PIC) calculation solves this system of equations self consistently including appropriate geometry, initial and boundary conditions with as few approximations as possible.

In the pFEL as discussed in this thesis, an electron beam with a current in the order of 1 A has to be considered. Such a beam current implies that approximately 1 billion electrons are simultaneously present in the interaction volume. Although computing power has undergone an enormous growth, such a number of particles require resources not yet available. Therefore, PIC algorithms make use of so-called super particles, which combine a number of electrons into a single particle. Due to their relatively large charge compared to electrons, the dynamics of mutual collisions is affected. To solve this problem, super particles are assumed as electron clouds with a finite and rigid size which may freely pass through each other.

The PIC algorithm calculates the electric and magnetic fields at each time step. Therefore, the time step in the PIC algorithm has to be sufficiently small to ensure numerical stability in the calculation. Each time step, the PIC algorithm calculates the fields from all particles and subsequently moves them. To illustrate the steps during each time step Figure 2.2 shows the subsequent steps. The particles are processed each time step Δt by four sub-steps. If one cycle is complete, the calculation has been progressed by Δt. Note that during each time step, all grid points and all particles need to be processed individually. Despite the use of super particles, both quantities are still in the order of 10^5–10^6, requiring high-end computers to achieve a reasonable computation time (several days).

To get a better impression of what happens each time step, let us discuss one cycle of the time step for a single particle in detail. We assume that the position and velocity of that particle is

known. This is the case when we move from the top box to the right box in Figure 2.2. In the right box, the charge density and the current density at the field grid points are calculated from the position and velocity of the particle. This requires a weighting, because the particle space is continuous and the field grid points are discrete. Subsequently, from the space-charge density and current density, the Maxwell equations are used to solve for the electric and magnetic fields. From these fields the force exerted on the particle is calculated by the Newton-Lorentz equation (2.9). Also here weighting is required for calculating the force at the continuous positions of the particles, because the fields are only known at the grid points. From the calculated force exerted on the particle, a new velocity and position can be calculated completing the time cycle. For a typical calculation, 10^5–10^7 time steps are required. For more information, the reader is referred to [44].

Chapter 3

pFEL structure design

To theoretically study the fundamental physics of a pFEL we first need to devise a PhC which amplifies Cerenkov radiation. Furthermore, to facilitate an experiment with a footprint below a few m^2, we chose for an electron energy smaller than 20 keV. Thereby, the beam parameters as typical used for electron guns used in microwave tubes are in the order of 10 to 15 keV. Finally, a broad tuning range of the laser is desired. In this chapter we devise an appropriate PhC by calculating the Pierce impedance and subsequently the small-signal gain. The Pierce impedance can quickly be determined, as only the PhC eigenmodes needs to be calculated. This leads to a fast initial design method.

An endless variety of PhCs can be taken from literature and studied regarding their gain and frequency tuning in a pFEL. However, to provide sufficient gain for a start-up of low oscillation, a suitably slowed phase velocity (synchronism) and a strong longitudinal electric field are required. Obviously, not every PhC provides such properties. To find an optimal PhC it is useful to define a measure to compare the different crystals. For such a measure we focus on gain and frequency tuning.

The small-signal gain, G, expressed as gain per wavelength, is retrieved from the Pierce theory. Although originally developed for classical slow-wave structures (SWS) far from cut-off, this theory can estimate the small-signal gain of photonic crystals as well. The Pierce impedance describes how strong the synchronous spatial harmonic E_z component is per unit power of the total radiation wave and is a measure for the coupling between wave and field. The gain per wavelength is calculated from the electron beam parameters through the beam impedance, Z_b, and from the wave properties through the Pierce impedance, Z_p.

Further we desire a broad tuning range. Tuning in output frequency of a pFEL is achieved by changing the acceleration voltage of the electron beam. Due to the PhC dispersion, the matching between the plasma wave and the eigenmode of the PhC appears at a different wave number and hence a different frequency is generated. We define the tuning range via the maximum and minimum frequency accessible by the given acceleration voltage of the electron source (10 - 15 kV)

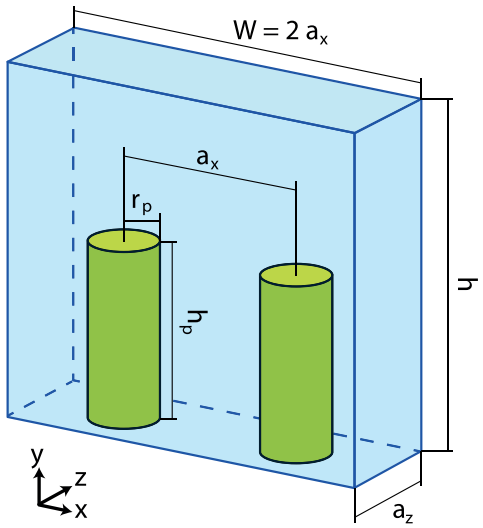

Figure 3.1: *Unit cell of the truncated post photonic crystal slab. The posts are made out of metal where the rest of the unit cell is vacuum.*

as

$$T = 2\frac{\nu_{max} - \nu_{min}}{\nu_{max} + \nu_{min}}. \tag{3.1}$$

In the following we show how we maximize the tuning range, T, and the small-signal gain per wavelength, G, simultaneously. First we describe the calculation method and then we optimize the most suited concept.

3.1 The truncated posts photonic crystal

In extensive calculations, we have investigated numerous different PhC designs to find the most suitable PhC for the pFEL. The investigated structures include dielectric, metallic and metallo-dielectric types. Here, we limit ourselves to the specific type of PhC that we indentified to show the best performance regarding gain and frequency tuning. In the unit cell of this PhC shown in Figure 3.1, two metallic posts are placed in a rectangular pattern inside a metallic waveguide [45]. As the posts do not extend along the entire height, we term this structure the truncated posts structure. The posts are of equal height, h_p, and radius r_p. Furthermore, the unit cell dimensions are determined by the height, h, the width, $W = 2a_x$ and the longitudinal lattice constant a_z. Table 3.1 gives the set of parameter values which are used in the following of Section 3.1.

To study the truncated posts PhC in terms of gain and frequency tuning we require the dispersion and eigenmodes. This can be done by an eigenmode solver [46]. Such calculations are greatly simplified by applying periodic boundary conditions at the edge of the unit cell (here in the z-direction), which implies that the structure is considered as infinitely long in the z-direction.

Design parameter	h	a_x	a_z	r_p	h_p
Parameter value	8	4.2	2.5	0.75	5

Table 3.1: *Typical parameters for the unit cell shown in Figure 3.1 for a pFEL operating at microwave frequencies. All units in mm.*

To calculate the dispersion of an infinitely long structure, the phase difference, φ_0, of the electromagnetic field between the front and the back of a single unit cell is varied. As $\varphi_0 = k_0 a_z$ and a_z is constant, this means effectively that the wave number is varied. Note that when φ_0 is set, not only a phase difference φ_0 fulfills the boundary conditions, but at the same time also all φ_m with

$$\varphi_m = \varphi_0 + 2\pi m, m \in \mathbb{Z}, \varphi_0 \in [-\pi, \pi)\,. \tag{3.2}$$

This is actually required because all spatial harmonics of an eigenmode need to be present to fulfill all boundary conditions in a periodic structure (see Section 2.3). To solve this eigenmode problem and retrieve the electromagnetic fields and corresponding frequencies for a given wave number k_0 we apply an iterative technique.

As we solve the problem for k_0, it is simultaneously also solved for k_m, because

$$k_m = k_0 + 2\pi \frac{m}{a_z}, m \in \mathbb{Z}, \tag{3.3}$$

hence, the band diagram is periodic. Note that, since gain only appears when eigenmodes with a longitudinal electric field component overlap with the electron beam, we limit ourselves to such eigenmodes. Figure 3.2(a) shows the band diagram of the three lowest order eigenmodes which have a longitudinal field component, E_z, along the PhC central z-axis for the unit cell shown in Figure 3.1. The -1^{st} to 1^{st} spatial harmonic is depicted in Figure 3.2(a). The vertical dashed lines mark the edges of the 0^{th} order spatial harmonic. The shaded area indicates the range where matching between the slow space-charge wave and PhC modes is possible. More specifically, the lower and upper boundary of the shaded area correspond to the slow space-charge wave dispersion for a beam energy of 10 keV and 15 keV, respectively. The Pierce impedance is inversely proportional to the group velocity, which is shown in Figure 3.2(b) as a function of wavenumber for a single Brillouin zone. Since the band diagram of the PhC is periodic, the group velocity is periodic as well with the same periodicity $2\pi/a_z$.

At the frequencies where the shaded area overlaps with the band diagram, coherent radiation can be generated and tuned with the electron beam energy. For example, Figure 3.2(a) predicts for mode 1 a tuning range T = 0.04. Note that slow space-charge wave intersects also with the other eigenmodes. The electron beam would in principle be able to interact with all modes. However, the interaction would then take place at higher wave numbers, k_z, and higher group velocity, v_g. It turns out that this drastically reduces the small-signal gain and we will thus neglect higher order modes.

To determine the Pierce impedance it is necessary to calculate the longitudinal electric field

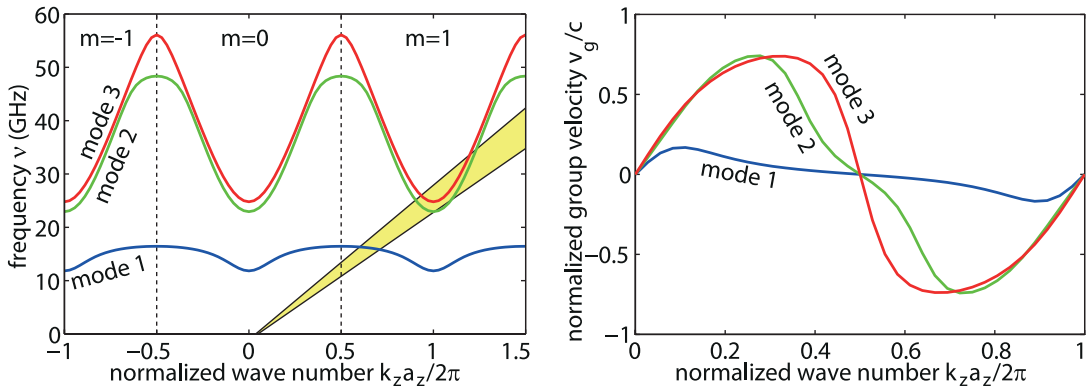

(a) (b)

Figure 3.2: *(a) The band diagram of the truncated posts PhC for the three lowest order modes with $E_z \neq 0$. The dashed lines separate the 0^{th} order spatial harmonic from the -1^{st} and 1^{st} order spatial harmonic. (b) shows the group velocity for the same modes.*

strength $E_z(k_0)$ from the total electric field $\mathbf{E}(k_0)$ where the spatial harmonic of the eigenmode is velocity matched with the slow space-charge wave. Furthermore, only the area of the field that overlaps with the electron beam will contribute to the interaction. To calculate the velocity matched field we have to decompose the total longitudinal field, given by the numerical eigenmode calculations, into a series of spatial harmonics. In general this is required for all transverse coordinates (x, y). To illustrate this decomposition, we consider the longitudinal field $(E_z(x = 0, y = 0, z))$, corresponding to the axis of the electron beam and axis of the waveguide, as a function of z. Figure 3.3(a) shows the longitudinal electric field $E_z(z)$ versus the normalized longitudinal position inside the PhC at a phase difference $\varphi_0 = -0.5\pi$, retrieved from the numerical calculations. Such a phase represents a wave number of $k_0 = -.5\pi/0.0025 = -628.3$ m^{-1}, which corresponds to a wavelength of $4a_z = 10$ mm. Indeed, the wavelength of the electromagnetic field shown in Figure 3.3(a) is 10 mm. Furthermore, small ripples repeating every $4/3a_z$ are visible, which are due to the 1^{st} spatial harmonic.

To decompose the electric field into different spatial harmonics a spatial Fourier transformation is performed using a fast Fourier transformation (FFT) algorithm. Figure 3.3(b) shows the resulting Fourier decomposition of the wave depicted in (a). According to Equation 3.2 in normalized wave numbers, only a single peak should occur every integer number. However, due to the nature of the FFT algorithm, which is not fully identical with a standard Fourier transformation, additional non-physical peaks occur. Because the physical wave number values have to be multiples of $2\pi/a_z$, and we know that the fundamental wave number k_0 is negative ($\varphi_0 = k_0 a_z = -0.5\pi$), the higher order spatial wave numbers can be found with Equation 3.3. The physically correct wave numbers are indicated with the black k's at the top of Figure 3.3(b). The k's on the bottom in gray give the wave numbers which are an artifact of the FFT algorithm. The correct wave numbers k_{-1}, k_0, k_1 and k_2 exactly match the phase differences given by Equation 3.2. Note that the amplitude of the

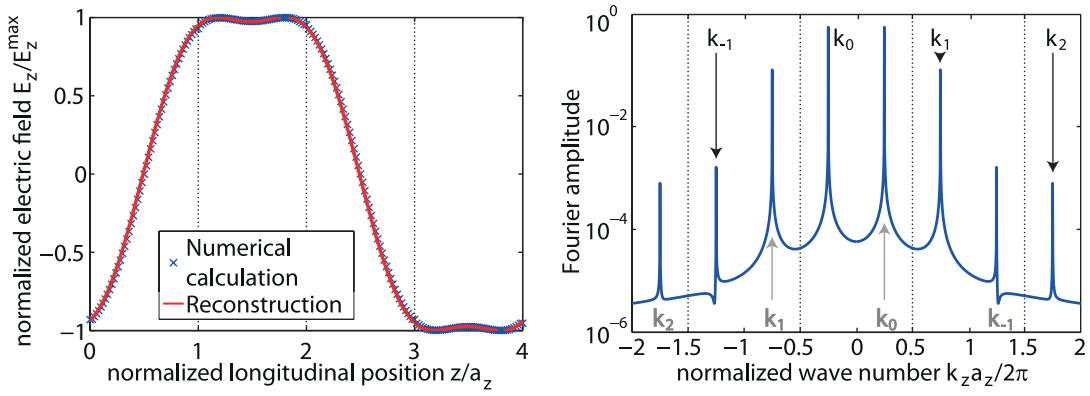

(a) (b)

Figure 3.3: *(a) The normalized amplitude of the electric field at the transversal center axis of the PhC (x, y) versus the normalized longitudinal position. The phase difference φ_0 is -0.5π, so one wavelength equals $4a_z$. (b) The double sided amplitude spectrum is plotted versus the normalized wave number.*

spatial harmonics drops as k_z becomes larger, which is disadvantageous for the Pierce impedance. Only an interaction with the fundamental or at most the first spatial harmonic leads to a sufficiently high gain to build useful devices.

To test the fidelity of our decomposition algorithm we reconstruct the original spatial field by using the calculated spatial Fourier amplitudes for the wave numbers k_{-1}, k_0, k_1 and k_2. In Figure 3.3(a) the reconstruction (solid line) is in good agreement with the original eigenmode solver data from CST (data points indicated with crosses).

Using the described decomposition algorithm for all transverse coordinates gives the transverse amplitude distribution for $E_{z,k_m}(x, y)$ at different spatial harmonics for a given k_0. Figure 3.4 shows the transverse amplitude patterns $E_{z,k_m}(x, y)$ for the spatial harmonics $n = -1, 0, 1, 2$. The dashed circle in the middle indicates the location of the electron beam. Also, the transverse location of the truncated posts are indicated in each figure with the dashed rectangles. The electric field amplitude of the 0^{th} order spatial harmonic is highest at the transverse coordinates where the posts are positioned. For the higher wave numbers, the electric field is almost entirely concentrated at the transverse post location. Note that this does not mean that an electric field is present inside the metallic posts. Figure 3.4 merely shows transverse amplitudes. When the total E_z field is reconstructed form the Fourier series, this will result in a zero field amplitude inside the metallic posts. However, for the interaction with an electron beam only a part of the electric field is responsible. As can be seen in Figure 3.4, the overlap between a particular spatial harmonic amplitude and the electron beam is maximized for m = 0. Furthermore, the maximum field amplitude decreases for higher wave numbers (Figure 3.3(b)).

From the Fourier decompositions of the eigenmodes we can calculate the Pierce impedance (2.23). The Pierce impedance versus normalized wave number is shown in Figure 3.5(a). Note

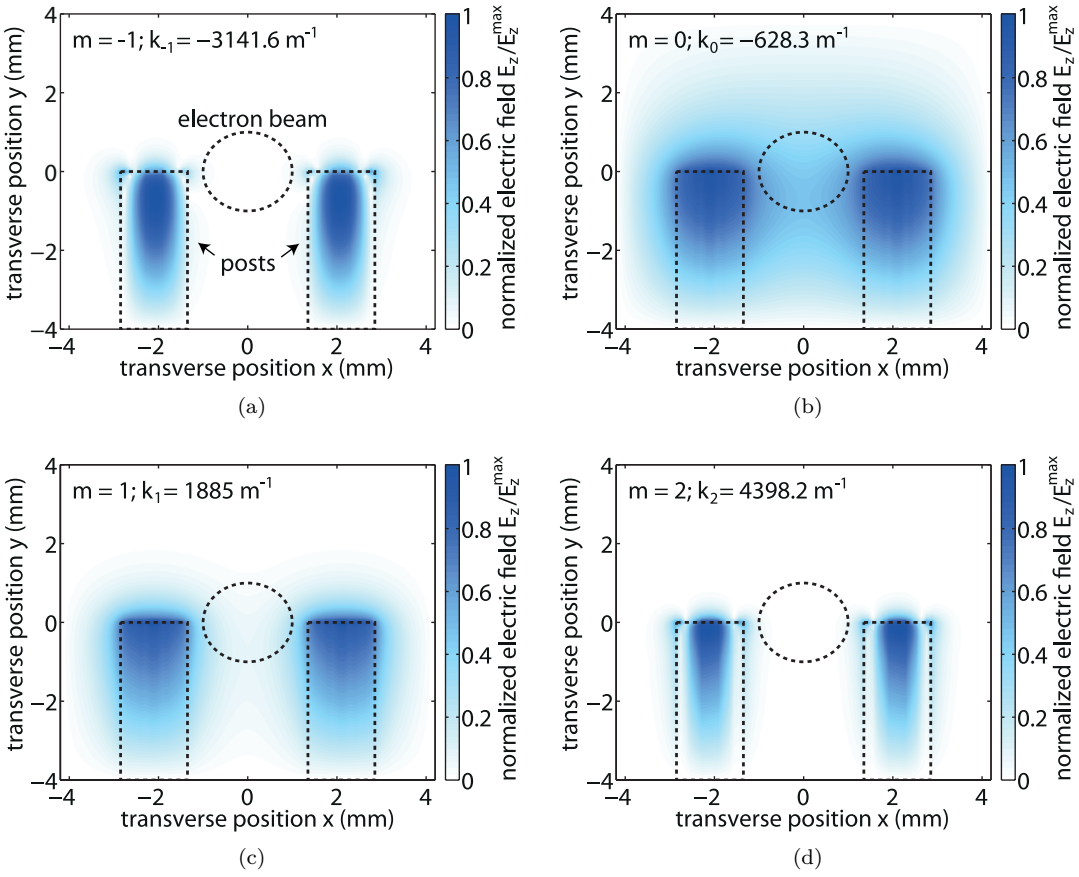

Figure 3.4: *Transverse electric field patterns $E_{z,k_m}(x, y)$ for m is (a) −1, (b) 0, (c) 1 and (d) 2. $k_0 = -.5\pi/a_z = -628.3\ m^{-1}$. All amplitude patterns are normalized to it's own maximum.*

that the 0^{th} order spatial harmonic (m = 0) is accessible at the left of the vertical dashed line and the 1^{st} order spatial harmonic (m = 1) is found at the right of the vertical dashed line. Note that there is a gap in the curve around the normalized wave numbers where the group velocity is zero (in Figure 3.5(a) at normalized wave numbers 0, 0.5 and 1). Mathematically this is because as the group velocity goes to zero, the Pierce impedance goes to infinity, which is non-physical. From the Pierce impedance, the gain per wavelength is calculated (Equation 2.21), which is shown in Figure 3.5(b). From the band diagram and the chosen acceleration voltages, we know that velocity matching can be achieved at normalized wave numbers between 0.6 and 0.7. It can be seen that in this range the gain is between 1.5 and 2.5 dB per wavelength.

To maximize the Pierce impedance, a velocity matched interaction point at a low wave number together with a low group velocity is favorable. The wave number at the velocity matched point is lowest for the lowest order eigenmode (see Figure 3.2(a)). For this eigenmode, the group velocity is lower than for the higher order eigenmodes (see Figure 3.2(b)). Because the Pierce impedance is maximized when the longitudinal electric field is maximized, it is favorable to have the velocity

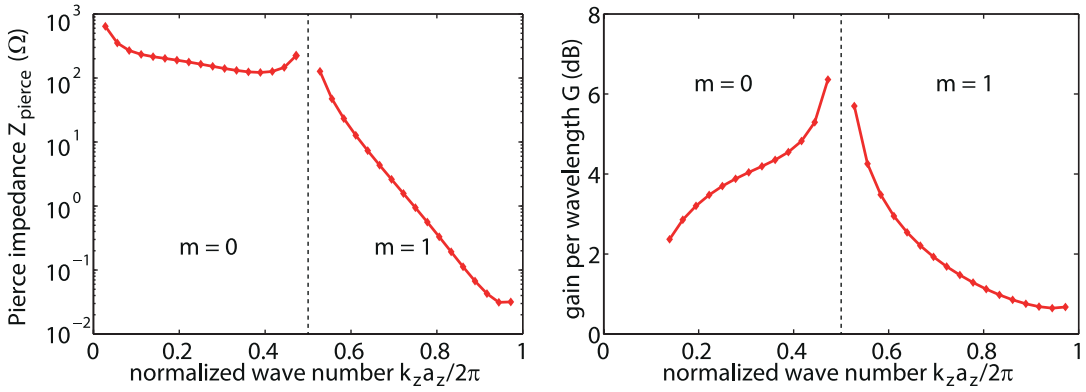

Figure 3.5: *(a) The absolute value of the Pierce impedance versus wave number. (b) The gain per wavelength versus wave number. Both (a) and (b) are for the structure shown in Figure 3.1 and parameters from Table 3.1. The solid line is drawn to connect the data points.*

matched point in the 0^{th} order harmonic. However, this requires a significantly higher electron velocity (see Figure 3.2(a)). Therefore, for the chosen acceleration voltages the slow space-charge wave interacts with the 1^{st} spatial harmonic. From Figure 3.2(a) we observe that for the given pFEL structure and beam voltages considered, higher order eigenmodes require interaction in higher spatial harmonics. This means that both the longitudinal wave number increases and the phase-matched spatial harmonic amplitude decreases. Furthermore, the group velocity usually increases for higher order eigenmodes as well. Together this means that, for this structure, higher order eigenmodes will experience a much lower gain and these are therefore not expected to grow. For this reason only the lowest eigenmode will be considered in the remainder of this thesis.

3.2 Photonic crystal optimization

To optimize the truncated posts PhC, the parameters indicated in Figure 3.1 are varied. Different parameter configurations are investigated in terms of tuning range and small-signal gain. To compare the different parameter configurations, only a single parameter is varied at a time.

As we already indicated in the beginning, we optimize the PhC such that we try to simultaneously increase the tuning range and small-signal gain. This requires to calculate the band diagram and eigenmodes for variations of the different parameters. Figure 3.6(a) shows the dispersion of the lowest order eigenmode for different post heights together with the dispersion of the slow space-charge wave. As before, the lower boundary of the shaded area (indicated with a black line) represents the slow space-charge wave of a 10 kV electron beam. The upper black line represents the dispersion when the electrons are accelerated to 15 kV. At the intersection of the radiation wave dispersion with the electron beam slow space-charge wave dispersion we expect gain. Several interesting features can be observed. First, the operating frequency increases, for

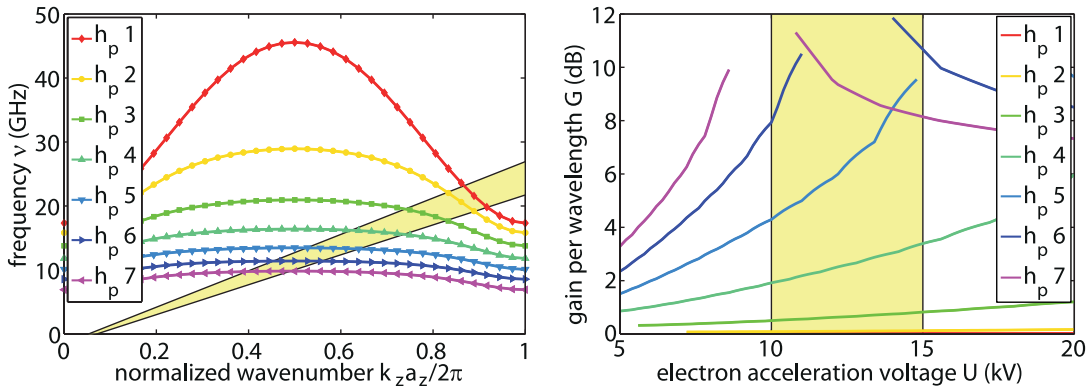

(a) (b)

Figure 3.6: *(a) The lowest order eigenmode band diagrams for variations on the post height together with dispersion of the slow space-charge wave for acceleration voltages between 10-15 kV. (b) The gain per wavelength as a function of electron acceleration voltage variations on the post height. Note that the shaded area in (b) represents to the dispersion of the slow space-charge wave in (a) between 10-15 kV.*

a given beam voltage when the post height deceases. Second, for a beam voltage of 15 kV, the interaction starts out as a forward wave interaction for the largest post height and is a backward wave interaction for the lowest post height. Third, the tuning range, T, as defined by Equation 3.1, increases with decreasing post height. This tuning range is plotted in Figure 3.7 as a function of the post height. Finally, the group velocity increases with decreasing post height. To conclude, the post height can be used to control the tuning range of the pFEL. As the small-signal gain per wavelength, G, depends on both the group velocity and phase-matched spatial harmonic wave number, and Figure 3.6(a) shows that these parameters change in a nonlinear way with the post height, we expect the gain to be a nonlinear function of the post height. This can be observed in Figure 3.6(b), where G is plotted as a function of the acceleration voltage for the electrons for various post heights. Indeed, Figure 3.6(b) shows that gain changes nonlinearly with the post height. In part this is due to the change in group velocity and in part due to change in phase-matched spatial harmonic wave number. The gain significantly decreases as the post height is deceased. Both figures 3.6(a) and (b) show that tuning range can be increased at the expense of gain and vice versa.

A Similar analysis has been performed for the other structure parameters like a_z and r_p. However, the value of a_x (4.2 mm) is set by the size of the electron beam (beam radius of 1 mm) and a minimum safe distance between electron beam and posts to allow transport of the electron beam through the structure. For the remainder parameters it was found that variation had only a minor effect on the tuning range and the small-signal gain (by at least an order of magnitude smaller change). Finally, for a first experimental demonstration, both a sufficient gain and a reasonable tuning range is desirable. The final design parameters for the PhC which can be

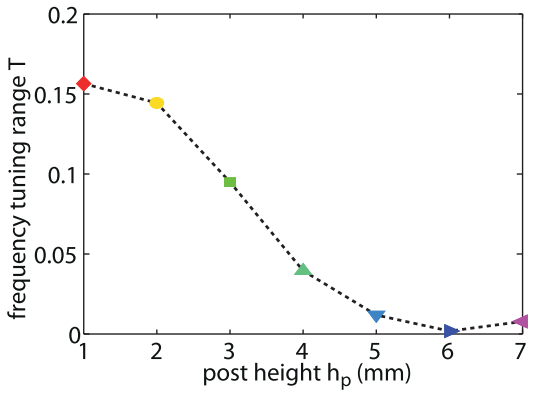

Figure 3.7: *The frequency tuning range calculated for several post heights.*

Design parameter	h	a_x	a_z	r_p	h_p
Parameter value	8	4.2	2.5	0.75	4

Table 3.2: *Final design parameters for the truncated posts design shown in Figure 3.1. All units are in mm.*

used in an experimental pFEL are shown in Table 3.2.

Chapter 4

Start-up and oscillation of a pFEL

To demonstrate that start-up of laser oscillation of a pFEL should be possible, and to investigate the basic physics and properties of this laser, we use the particle-in-cell (PIC) method. For our investigations, which include also the nonlinear dynamics, such as steady-state operation based on gain saturation, we consider the PhC we have presented in the previous chapter.

The results from the eigenmode calculations should allow to predict, at least approximately, the laser oscillation frequency and wave number obtained by the PIC calculations. In addition, the electron beam dynamics are investigated, i.e., electron bunching, especially in its start-up phase. We begin by comparing the results obtained from the linear model with results obtained from a PIC calculation for a single electron beam velocity. Subsequently, we demonstrate the frequency tuning by varying the acceleration voltage. Using the same model, the beam voltage is varied between 10 kV and 15 kV. A comparison is made between the expected output frequency from eigenmode calculations and the PIC calculations.

4.1 Laser output

To investigate start-up and transition to steady-state oscillation of the pFEL a PIC model is set-up which is shown in Figure 4.1. The gain section of the pFEL is formed by 20 PhC unit cells. The unit cell is described in detail in Section 3.2. Through the PhC an electron beam is propagating at the transverse center of the unit cell, as was indicated in Figure 3.4. The radius of the cylindrical electron beam is 1 mm, the beam current is 1 A and the acceleration voltage is 12.5 kV. An ideal electron beam is assumed for the PIC calculations. Guiding of such a beam is achieved by a homogeneous, longitudinal magnetic field B_z, with a strength of 0.5 T. We place the gain section inside a resonator, which is formed by a flat metallic mirror at A and a partial reflecting mirror at B. The reflectivity at B is due to the transition from the PhC slab to the empty output waveguide. Both mirrors at A and B provide the resonator with a total round-trip reflectivity of approximately 95%. The output waveguide between B and C is twice as wide as the PhC slab to allow extraction of the generated radiation. We note that, with an output waveguide with the same

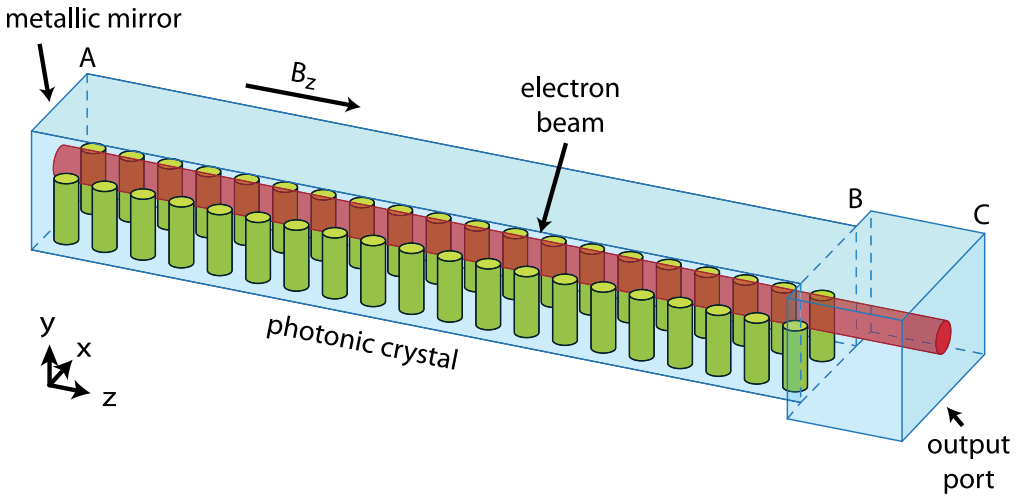

Figure 4.1: *The PIC calculation model. Here, two rows of metal posts are place inside a rectangular metallic waveguide. The rest of the volume inside the waveguide is assumed to be vacuum.*

width and height as the PhC slab, the generated radiation could not propagate through the output waveguide. The reason is that the cut-off frequency of a waveguide is lowered by the presence of metallic rods. At C the output power is sampled at the so-called output port, which pervents any back-reflections from this plane. Furtermore, in the plane of the output port, the electromagnetic field is decomposed into the modes of the empty rectangular waveguide between B and C.

The PhC supports only a single mode for frequencies below 20 GHz as illustrated in Figure 4.2(a). This figure shows the band diagram of the lowest order mode with $E_z \neq 0$ at the PhC center. The lowest frequency of the next higher order mode with $E_z \neq 0$ is higher than 20 GHz. Furthermore, the cut-off frequencies of the empty waveguide modes in the output waveguide (horizontal dashed lines) and the slow space-charge wave dispersion of the electron beam (tilted solid line) for an energy of 12.5 keV and 1 A are shown. As the figure shows, the expected operating frequency of 16 GHz is only supported by the TE_{10} mode in the output waveguide. Therefore, we expect any laser output at C only to appear in the TE_{10} mode.

The average calculated output power versus time in the TE_{10} mode at the output port is shown in Figure 4.2(b). Initially no radiation is inside the resonator. Shortly after the electron beam is slowly turned on at t = 0 with a rise time of 0.1 ns, it can be seen that noise-like radiation is generated. After about 10 ns an exponential growth is observed, indicated by the straight line in the logarithmic plot. After 40 ns the growth reduces, indicating that the gain starts to saturate. Finally the growth stops completely and the output power settles down to a steady-state power of 1475 W. At this point the gain exactly compensates the losses per round trip. We note that the power versus time in Figure 4.2(b) only represents the temporal development of the envelope of the laser field. The actually observed field (not shown) consists of a regular, sinusoidal oscillation growing out of initial noise, with an oscillation frequency of about 16 GHz, following the power envelope of Figure 4.2(b).

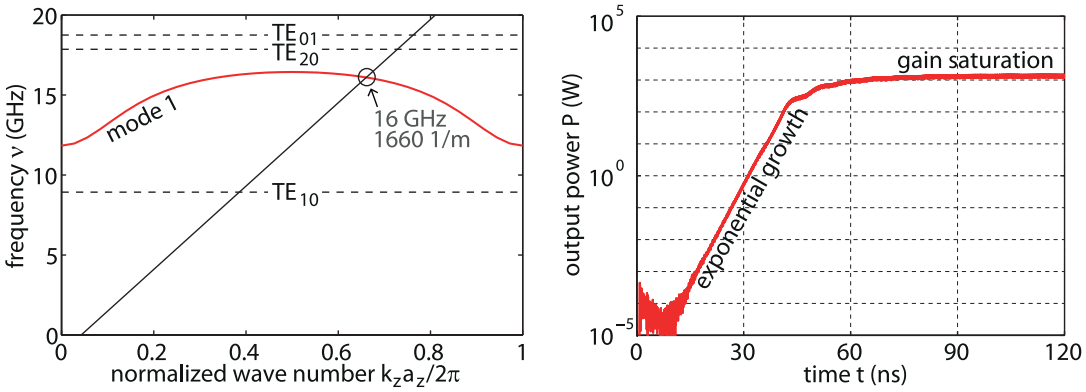

(a) (b)

Figure 4.2: *(a) The band diagram of the PhC together with the cut-off frequencies of the empty waveguide modes in the output port and the dispersion of the slow space-charge wave. (b) The output power in the TE_{10} mode monitored at* C.

A small part of the output power is also contained in higher order empty waveguide modes. However, the total power in higher order empty waveguide modes is at least over four orders of magnitude lower than in the TE_{10} mode. Hence, it can be concluded that the output power of the pFEL is to very good approximation in a single spatial mode of the output waveguide. The following part of this chapter will focus on the pFEL output in the TE_{10} mode.

From the eigenmode calculations (linearized model) it is expected (Figure 4.2(a)) that the operating frequency of the output signal in the TE_{10} mode is 16 GHz. To investigate the validity of the linear approximation, we compare this with the results from the PIC calculations (nonlinear model). Figure 4.3(a) shows the laser output spectrum of the TE_{10} mode as obtained from the PIC model. The output spectrum is calculated by performing a Fourier transform of the fully time resolved signal of the TE_{10} output. It can be seen that the peak in the amplitude spectrum is located at 15.96 GHz and has a full width half maximum (FWHM) of 20 MHz. The operating frequency from the PIC calculation is in good agreement with the expected frequency of 16 GHz from the eigenmode calculations.

An important feature of the pFEL is its high spectral coherence, which can be seen from the relatively narrow spectral bandwidth of the output shown in Figure 4.3(a). Such narrow bandwidth is presumably the result of spectral condensation during the start-up phase of the laser. To investigate such spectral condensation, we have divided the laser output field into a series of time windows of 4 ns duration. A Fourier transform is performed on each window. Note that our choice of the division of the window limits the spectral resolution to 0.25 GHz. Figure 4.3(b) shows the time evolution of the amplitude spectrum of the signal, in which frequency is plotted versus time. The color scale represents the normalized amplitude on a Decibel scale, normalized to the peak amplitude at t = 120 ns. One sees that during the first 10 ns a broad spectrum of output frequencies is generated as expected from noise-like and thus incoherent emission. After 10 ns until

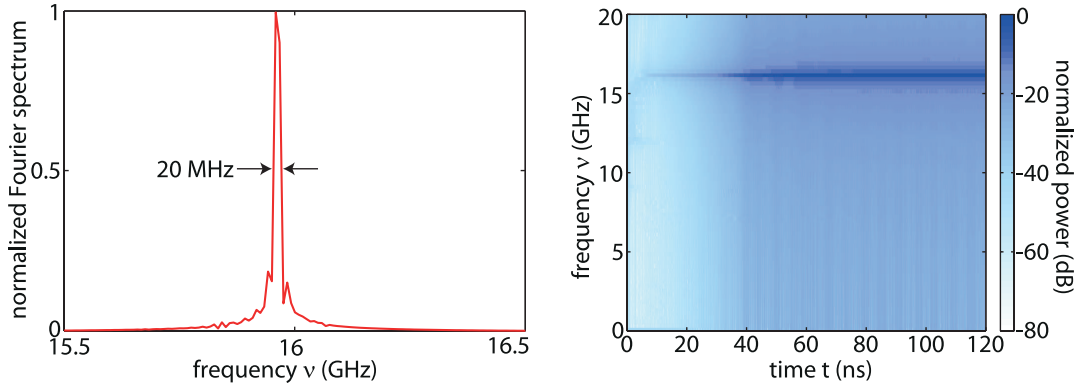

Figure 4.3: *(a) Frequency spectrum of the TE_{10} mode calculated from the complete simulation time and (b) the time evolution of the frequency spectrum.*

40 ns, where the exponential growth region is, the operating frequency grows much stronger than the neighboring frequencies slightly above and below 16 GHz. When the output power saturates, the pFEL operates as a stable amplitude laser at a stable frequency and with a stable bandwidth.

In any FEL temporal coherence is observed when the initially continuous stream of electrons becomes spatially structured in the form of so-called electron bunches, periodic in space and time. In more detail, the longitudinal electric field of the radiation wave exerts a periodic force (periodicity is $\frac{2\pi}{k_z}$) on the electrons. This force accelerates and decelerates electrons such that after some propagation the electrons will form bunches. These bunches are separated by the radiation wavelength in the PhC. The radiation emitted by successive electron bunches can constructively interfere, hence coherent radiation is generated. From the eigenmode curve in Figure 4.2(a) we retrieve a wave number of $0.66 \cdot 2\pi/a_z = 1660$ m^{-1}, which corresponds to a radiation wavelength of 3.8 mm inside the PhC for a frequency of 16 GHz. For comparison with the results from the PIC model, Figure 4.4 shows the line charge density as a function of position within the PhC slab for several instances in time during start-up of the laser. Initially (4.4(a)), the electron charge density is nearly constant, showing only some small fluctuations due to numerical effects. When the field starts to grow exponentially, at around t = 33 ns a spatially periodic modulation is observed (4.4(b)). Subsequently, the modulation is seen to become more pronounced. The modulation was determined via an auto-correlation method to possess a period length of 3.8 mm (4.4(c)). At the onset of saturation (4.4(d)), the electron beam is found to exhibit a second, additional modulation period. As saturation progresses, we observe a shift in the maximum modulation depth towards low z-coordinates, where the electron beam is injected. The described effects of bunching and saturation are actually characteristic and typical for free-electron lasers in general. Close to saturation, numerous additional frequency sidebands are generated in the electron density modulation. However, as we have limited the calculation frequency of the electromagnetic field

to values below 25 GHz in the PIC calculation, we are not able to observe if such high-frequency sidebands are present in the output of the pFEL.

4.2 Frequency tuning

To study the tuning of the pFEL we varied the acceleration voltage of the electron beam between 10 kV and 15 kV. The black curve in Figure 4.5 gives the operating frequency of the pFEL expected from the velocity matching between the slow space-charge wave and the PhC dispersion (synchronized mode). The center frequency obtained form a series of PIC calculations is indicated by the black crosses.

From the velocity matched operating frequencies we expect a continuous tuning. However, the frequencies calculated with the PIC model show a stepwise increase of the output frequency. A possible explanation of such stepwise increment is the following. As discussed in the beginning of this chapter, the PhC is embedded inside a resonator, which extends form A to B as shown in Figure 4.1. This limits the possible emission frequencies to the longitudinal resonances of the resonator and to corresponding longitudinal eigenfrequencies, leading to this stepwise increase in output frequency tuning. This phenomenon is actually well-known as mode hopping. The same phenomenon is observed in all other tunable lasers, such as fiber or diode lasers for the optical range. Also, for all PIC calculations away from the stepwise increments we observed a bandwidth of 20 MHz.

Figure 4.5 shows that, when neglecting the small deviations caused by longitudinal mode hops, the Pierce theory is able to predict the operating frequency of the pFEL with a rather high precision. Because eigenmode calculations of a PhC require far less time to perform than complete PIC calculations, the Pierce theory offers a powerful tool to quickly investigate the basic tuning capabilities of PhC used in a pFEL.

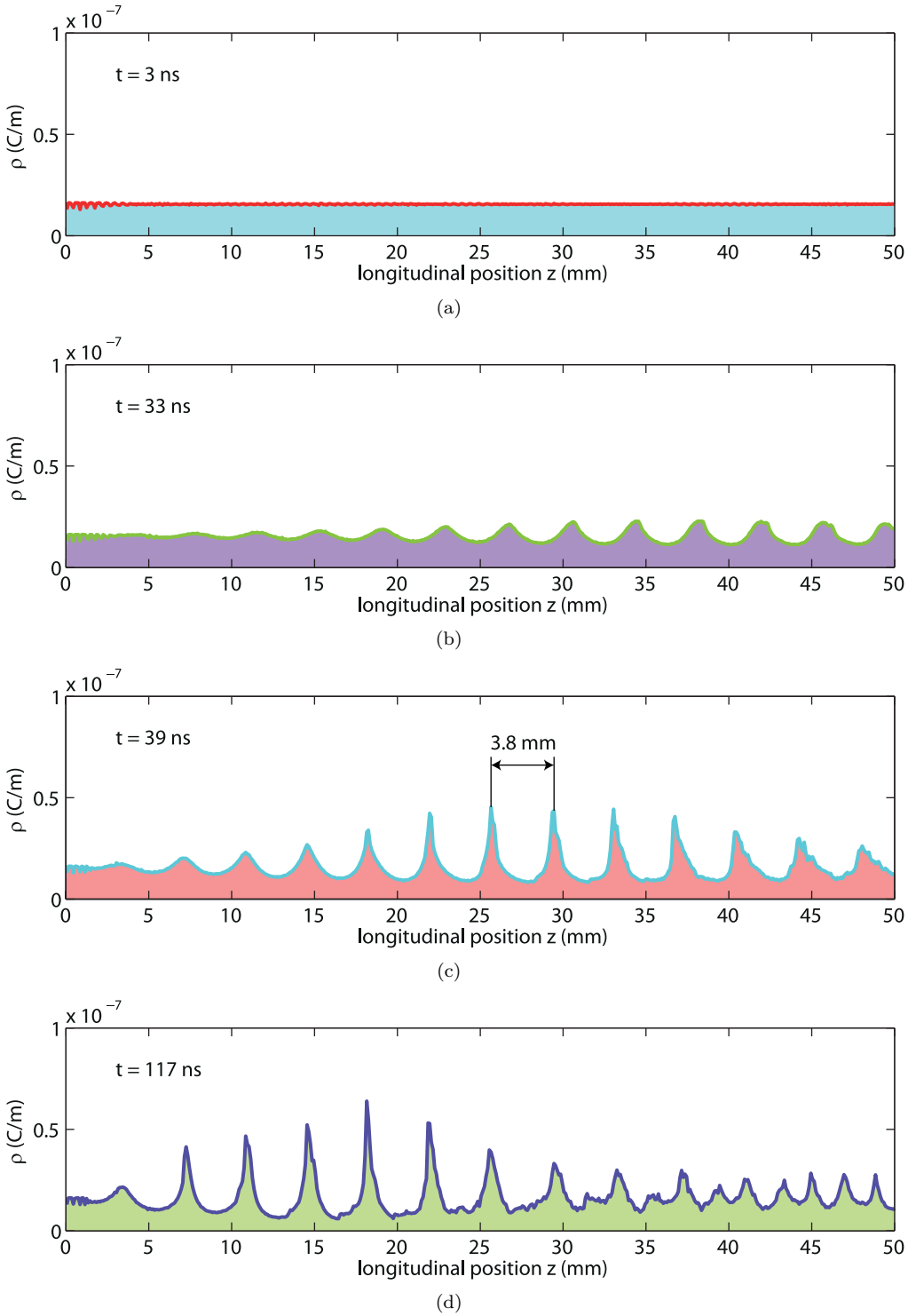

Figure 4.4: *The line charge density versus position at (a) t = 3 ns, (b) t = 33 ns, (c) t = 39 ns and (d) t = 117 ns.*

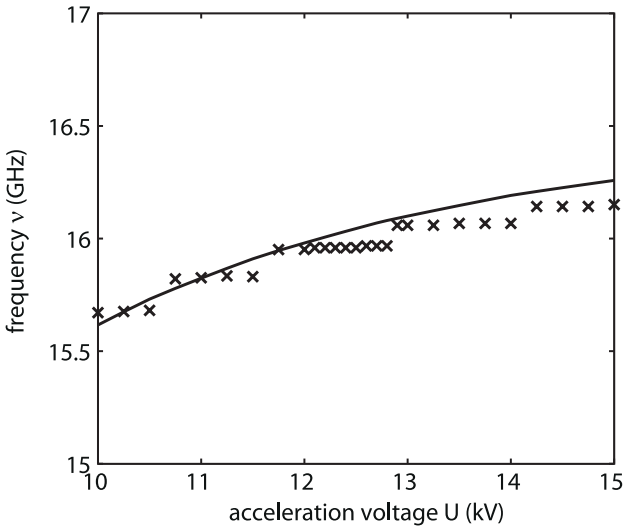

Figure 4.5: *The output frequency of the TE_{10} mode for different acceleration voltages. The black curve shows the frequency predicted by the linear approximation. The black crosses are the laser operating frequencies from the PIC calculations.*

Chapter 5

Transverse phase dynamics

The radiation produced in a pFEL scales with the number of electrons participating in the interaction. One way to increase this number is by increasing the electron density in the electron beam while keeping all other parameters constant. However, Coulomb forces between the electron will eventually limit the current density to preserve beam quality and beam transport through the PhC. The PhC allows for a second method, i.e., by keeping the current density and other parameters constant and increase the number of electron beams propagating in parallel through the PhC. The number of electron beams may even range up to tens of thousands, which is required if we want to scale to much higher frequencies.

Ideally, all electrons contribute constructively to the amplification process, i.e., the emission of all dipoles excited by the electrons is in phase with the existing field. For the pFEL, this means that the bunching taking place in all the beams must be phase locked. In case of an amplifier, a coherent seed injected into the pFEL can provide the locking of all the individual beams to the phase of the seed. In case of an oscillator, as we are studying here, initially no radiation field is present and the laser starts from noise. Therefore, initially the individual electron beams will evolve independently. However, as the electrons induce spontaneous emission, each individual beam will experience the fields generated by the other beams and it is therefore expected that this feedback mechanism will eventually result in a single, coherent radiation field, and that the bunching in every one of the electron beams will be phase-locked by this common radiation field.

In this chapter we study the start-up dynamics in a multi-beam pFEL with emphasize on how quickly the electron beams become phase-locked to each other by the radiation field. We consider the most simple case of a two-beam array.

5.1 A two-beam array

For the two-beam pFEL we use a photonic structure as shown in Figure 5.1. The structure consists of two copies of the single-beam pFEL PhC structure as shown in Figure 3.1, placed at a distance d (measured from the center of each structure) from each other. For this study, d is taken to be 10

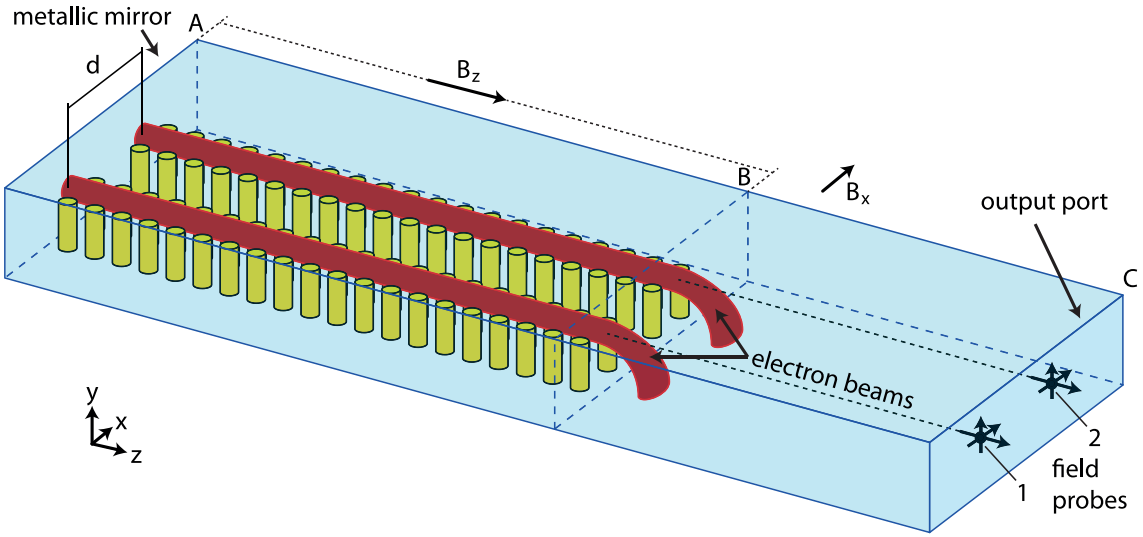

Figure 5.1: *Model used in the phase locking PIC calculations. The posts are modeled as metal whereas the rest of the volume of the waveguide is vacuum.*

mm and the width of the complete waveguide is 30 mm. The waveguide loaded with the PhC is followed by the output waveguide that has the same transversal dimension as the loaded waveguide and is sufficiently wide to make the cut-off frequencies of several empty waveguide eigenmodes to be below the frequency generated by the pFEL. This can be observed in Figure 5.2, where the band diagram of the PhC is shown for the three lowest order PhC eigenmodes with a non-zero longitudinal field. Also shown are the cut-off frequencies for various empty waveguide modes (horizontally dashed lines) and the dispersion of the slow space-charge wave supported by a 12 keV electron beam having a current of 1 A. Figure 5.2 shows that, a priori, the radiation generated in the PhC can couple to multiple empty waveguide modes when the power is transported to the output port.

The transition from the waveguide loaded with the PhC to the empty waveguide at B in Figure 5.1 again acts as a partial, in general frequency dependent, mirror and forms together with the metallic mirror at A a resonator.

The gain for this pFEL is provided by two identical electron beams, each having a current of 1 A at a beam voltage of 12 kV. To guide the electrons through the PhC, a homogeneous longitudinal magnetic field B_z with a strength of 0.4 T is applied. To analyze the radiation the field at the output port at C is decomposed into the eigenmodes of the port. However, to obtain more information about the phase of the field, two additional electric field monitors are placed 1 mm in front of the output port and in line with the electron beams.

To avoid that the field probes also measure the self-field of the electron beam, the guiding magnetic field is artificially ended at the end of the PhC and a transverse magnetic field B_x is applied immediately after the PhC to bend the electron beams into the waveguide wall. The distance from the dump position to the field probes is sufficiently large for the probes to measure

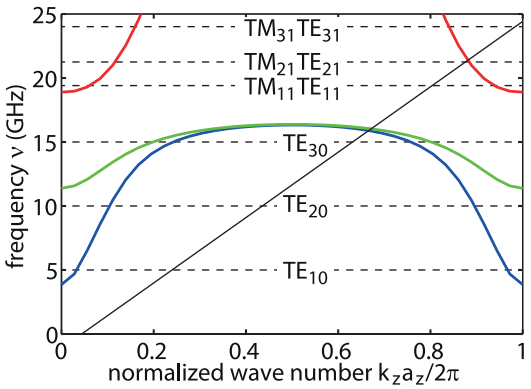

Figure 5.2: *The band diagram of the PhC together with the cut-off frequencies of the empty waveguide modes at the output port.*

only the electric field from the wave propagating through the output waveguide.

The band diagram in Figure 5.2 shows that the electron beam can interact with two closely spaced PhC eigenmodes at around 16 GHz. Calculating the small-signal gain for each of these modes shows that the lowest-order eigenmode should dominate the interaction.

5.2 Output power

As discussed in the introduction, the output power of a pFEL is determined by the number of electrons participating in the interaction. This can also be seen in the expression for the small-signal gain (Equation 2.21). If all electron beams would experience the same phase-matched field amplitude, then the Pierce impedance will be independent of the number of electron beams. However, as the transverse field will change with transverse position, the strength of the field will vary somewhat from electron beam to electron beam. As we keep the electron beam voltage constant and increase the total current by increasing the number of electron beams, the beam impedance will decrease (Equation 2.22). Consequently, the small-signal gain will increase (Equation 2.21), as we expect the Pierce impedance to decrease much more slowly than the beam impedance when the number of electron beams is increased for a well designed system.

To verify this line of reasoning, we have taken the pFEL geometry described in Section 5.1 and first turned on one electron beam and then both. The calculated output power is shown in Figure 5.3 as a function of time. We observe that when one beam is turned on, the saturated output power is approximately the same as for the single-beam pFEL studied in Chapter 4. The operating frequency is 15.9 GHz with a FWHM of 40 MHz. Despite the output waveguide being multi mode for the generated frequency, almost all the power is observed in the TE_{10} mode. The power observed in the next higher order mode is at least an order of magnitude lower.

When both beams are turned on, the multi-beam pFEL saturates at about twice the output power than when the same device is pumped by a single beam. Also, for this case an output

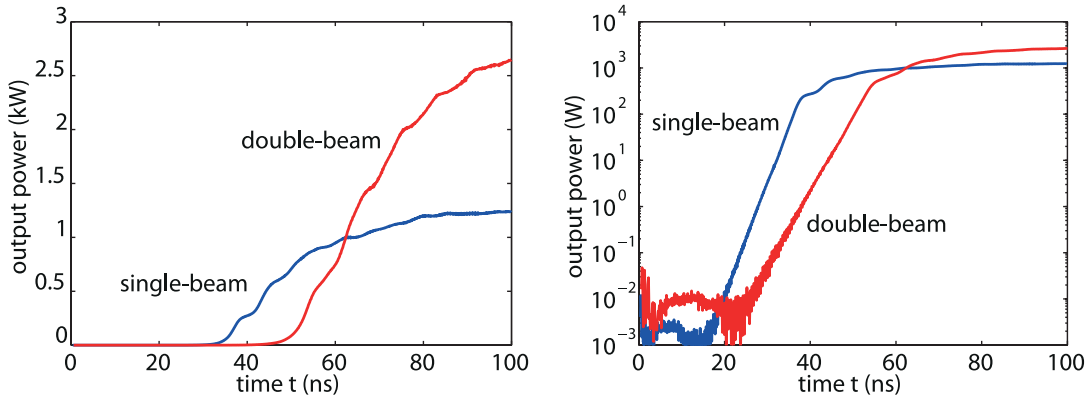

(a) (b)

Figure 5.3: *The output power versus time for a single-beam pFEL and a double-beam pFEL. Both calculations are performed using the same model as shown in Figure 5.1. For the single beam calculations only the first beam is turned on. In (a) the output power is plotted in kW on a linear scale, whereas in (b) the output power is plotted on a logarithmic scale in W.*

frequency of 15.9 GHz was produced with a FWHM of 30 MHz. The decomposition of the field into eigenmodes at the output port shows that almost all the power is in the TE_{10} mode. It is observed that the next higher order mode is over two orders of magnitude in power lower than the TE_{10} mode. Therefore, we can conclude that increasing the number of beams from one to two does not change the operating frequency, bandwidth and output mode, but is does approximately double the output power and actually improves the mode separation for the case studied. However, Figure 5.3 shows that up to 60 ns, the output of the pFEL pumped by two beams is below that of the same pFEL pumped by a single beam. Note, that in all these observations it does not matter which of the two beams is turned on when the device is pumped by a single electron beam. As we expect the two beam pFEL to have a higher gain, we expect it to grow faster. This is not observed in Figure 5.3. Also, it takes longer for the two beam case for the exponential growth to kick in, resulting in a longer time to reach saturation. It is therefore of interest to study the multi-beam laser dynamics in the start-up phase of the laser in more detail. This will be the subject of future work.

In the remainder of this chapter we will focus on how the phase front of the generated radiation is established and more particular, how robuust the wave front is if the electron beams start to deviate from being "identical".

5.3 Phase front observation through field probes

As is clear from the previous sections, the dynamics of a multi-beam pFEL can be complicated. The larger transverse extend required to propagate many electron beams in parallel leads to a so-called overmoded system. Multiple eigenmodes can interact simultaneously with the electron

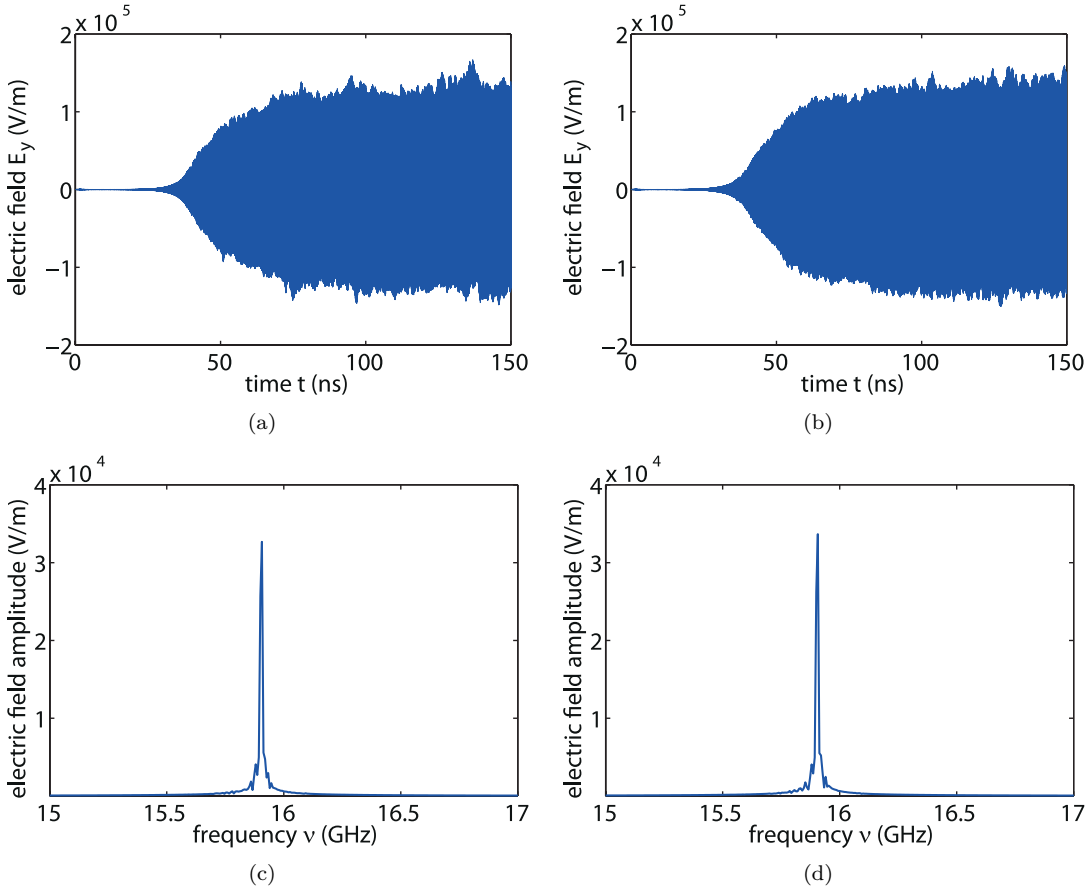

Figure 5.4: *E_y monitored at (a) probe* 1 *and (b) probe* 2*. Figures (c) and (d) show the Fourier transform respectively.*

beams and this may influence the coupling between the beams.

Here we want to investigate one aspect of this complicated dynamics and focus on the robustness of the phase front of the generated radiation when the electron beams start to deviate from being identical. A complete analysis could be made if the complete electric field distribution throughout the PhC and output waveguide would be available at all times during the calculation. However, the amount of data involved is gigantic and virtually impossible to store and manipulate. We therefore use two electric probes located in line with the two electron beams and just in front of the output port (see Figure 5.1). This allows us to record the electric field as a function of time at these two locations. From Figure 5.2 it is clear that the frequencies of interest generated in the PhC can only couple to propagating TE modes. Therefore, we can limit ourselves to the analysis of the E_y component as the E_y component completely describes the radiation in the output waveguide.

To describe the analysis method in more detail, Figures 5.4(a) and (b) show the E_y component as monitored by probes *1* and *2*, respectively. As a reference two identical electron beams, at least to the extend allowed by the PIC software, are used. Because the period of the oscillation is much

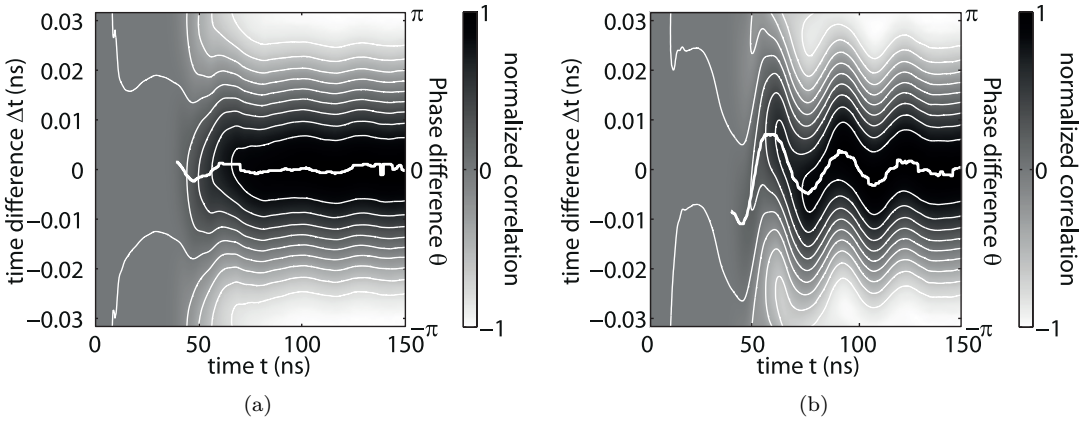

Figure 5.5: *(a) The time evolving cross correlation between the E_y field monitored at probe* 1 *and probe* 2*. The rise times of the current in both electron beam is equal to 0.1 ns. The correlation is normalized to the maximum correlation value. Contour lines at a step interval of 0.2 are added. The thick white line indicates the maximum value of the correlation from 40 ns. In (b) the same cross-correlation is performed where the rise time of the current for the second electron beam is equal to 10 ns.*

smaller then can be distinguished by eye, only the envelopes are visible in Figures 5.4(a) and (b).

The initially noise-like emission generated by the electrons is not visible on the linear scale used in these figures. Also, the exponential growth over many orders of magnitude is difficult to observe. At around 30 ns, saturation sets in and after about 60 ns a stationary output is obtained. The residual oscillations are due to electron-beam noise generated by bending the bunched electron beams.

A first analysis of these traces is made by applying a Fourier transform. Figures 5.4(c) and (d) show the amplitude of the spectrum obtained after the Fourier transformation for the E_y fields monitored at probe *1* and *2*, respectively. Both spectra show the same center frequency of 15.9 GHz and a FWHM of 30 MHz. The phase of the spectrum at the center frequency can give information about the phase front of the radiation. However, if one wants to study this dynamically, a moving time window is required in which the Fourier transform is performed. The reduced length of the time signal results in a loss of spectral resolution. Hence, we applied a cross-correlation method to study the time-dependent phase difference between the two probe signals.

Because the operating frequency, ν_0, is known and equal for both electric fields monitored at the probe positions, the phase difference can be calculated from the cross-correlation using

$$\theta = 2\pi\nu_0\Delta t. \tag{5.1}$$

Here, Δt is the time delay applied to calculate the cross-correlation. The cross-correlation between

the two probes is calculated as

$$h(\Delta t) = \int_{t_1}^{t_2} E_{y_1}(t) E_{y_2}(t + \Delta t) dt. \tag{5.2}$$

To obtain the temporal evolution of the cross-correlation we apply a moving time window to the calculation of the integral. Figure 5.5(a) shows the cross-correlation function as a function of time (or phase difference θ) using a temporal window of 4 ns, for the two probe signals shown in Figures 5.4(a) and (b), respectively. The cross-correlation is shown in a pseudo-color and is normalized to the maximum correlation value. Figure 5.5(a) shows that for the first 10 ns hardly any correlation is present. For the first 20 ns or so, this is due to the noise-like spontaneous emission generated by the electrons. After this time, exponential growth sets in and the spectrum starts to condensate. In this region the correlation is still low. After about 40 ns a correlation is visible, which becomes more pronounced as the laser reaches saturation. The thick white line in Figure 5.5(a) corresponds with the maximum in the cross-correlation, i.e., it gives the temporal trace of the phase difference, θ. From this we conclude that when the radiation has grown significantly above the spontaneous emission level, the spectrum of the two probes condenses to a single line and at about 40 ns there is only a small phase difference between the two probes. This phase difference then quickly drops to zero within 10 to 15 ns time.

It is interesting to investigate how the pFEL responds if the two beams are not identical. As a first step, we investigate here what happens if the rise time of the second beam will be a factor 100 slower (10 ns instead of 0.1 ns). We again first calculate the Fourier spectrum from the E_y fields monitored at the probes. As expected, the operating frequency is the same for both field probes. Again, we use the windowed cross-correlation to investigate the time dependent phase difference between the two probes. The result is shown in Figure 5.5(b). For the first 40 ns or so, the behavior is quite similar for the case with two identical beams. Again this is due to the initial noise-like emission of the dipoles and it takes time to spectrally condensate into a single frequency. At around 40 ns, a correlation is established between the two probe signals, including a phase difference of about 60 degrees between the two signals. This phase difference undergoes a damped oscillation with time and approaches zero at the end of the calculation time interval. Clearly, the different rise times of the electron beams affect the coupling between the beams, though eventually both pFELs (identical beams and different beams) produce very similar laser radiation.

5.4 Phase front observation through electron bunching

The phase behavior observed through the field probes only describes the phase difference between two particular fixed points. To obtain a complete phase front, many field probes need to be inserted and analyzed. However, it is much simpler instead to investigate the electron behavior. The bunching in the electron beam is responsible for aligning the dipoles responsible for emission of the radiation. Hence, for a maximum bunching, i.e., all electrons have the same phase with respect to the radiation, the dipoles induced by the electron bunches emit in phase and a coherent

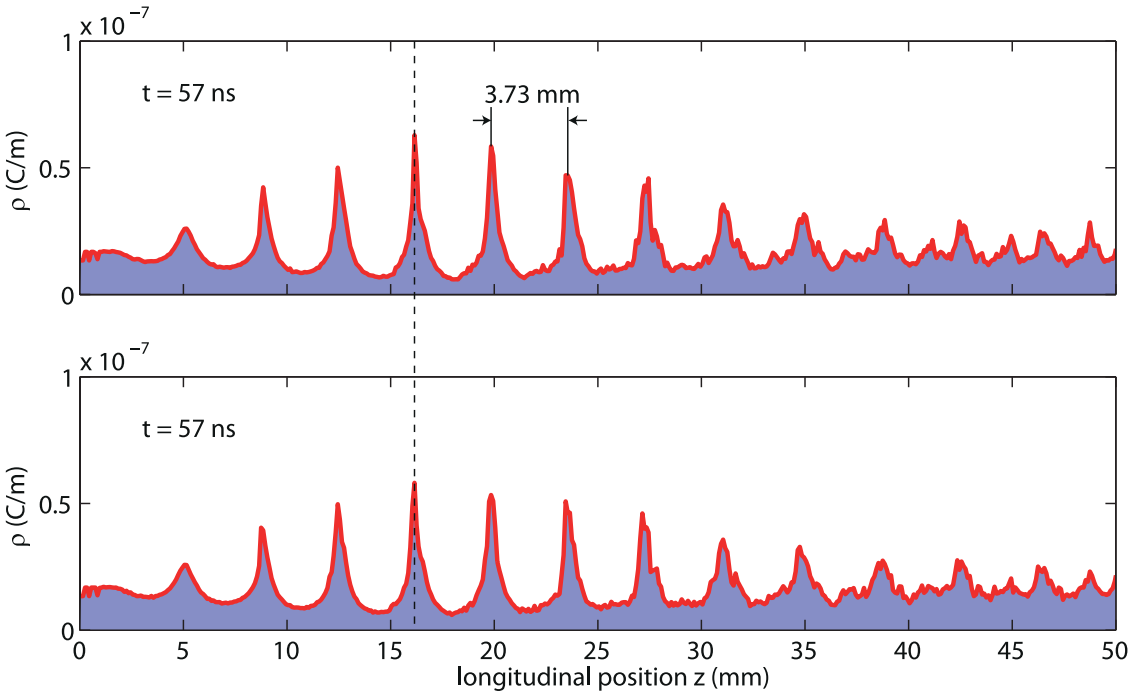

Figure 5.6: *The line charge density in the (top) first electron beam and (bottom) second electron beam at t = 57 ns. Both rise times of the beam current are equal.*

field with a single well defined phase will be generated. Thus by inspecting the bunching within the electron beams, in particular the level and location of the bunches, information of a possible phase difference between the electron beams can be observed.

As the bunching information is obtained over the whole length of the interaction volume (PhC), information about phase difference as a function of longitudinal position is obtained at a particular time. This in contrast to the phase difference as a function of time for a fixed position from the cross-correlation of the two field probe measurements discussed in the previous section. A so-called particle position monitor that stores the position of each individual particle at certain moments in time can be added to the PIC calculation to get information about the bunching. Again, due to the amount of data stored, the monitor only stores the position of the particles for a few moments in time. For both electron beams the bunching is investigated separately.

It is assumed that all electrons with $x < 0$ belong to the first (left) electron beam and all electrons with $x > 0$ belong to the second (right) electron beam. For each electron beam, the particle positions at a given time is condensed into a line charge-density. Figure 5.6 shows the line charge-density versus longitudinal position for the left beam (top) and the right beam (bottom). Similar as for the single beam pFEL, bunching occurs in the electron beams with a distance between successive bunches of 3.73 mm. The location of the bunches in the left beam overlap exactly with the location of the bunches in the right beam. This is emphasized by the vertical dashed line at $z \approx 16$ mm, at the location of the fourth electron bunch. The field probe measurement (Figure 5.5(a))

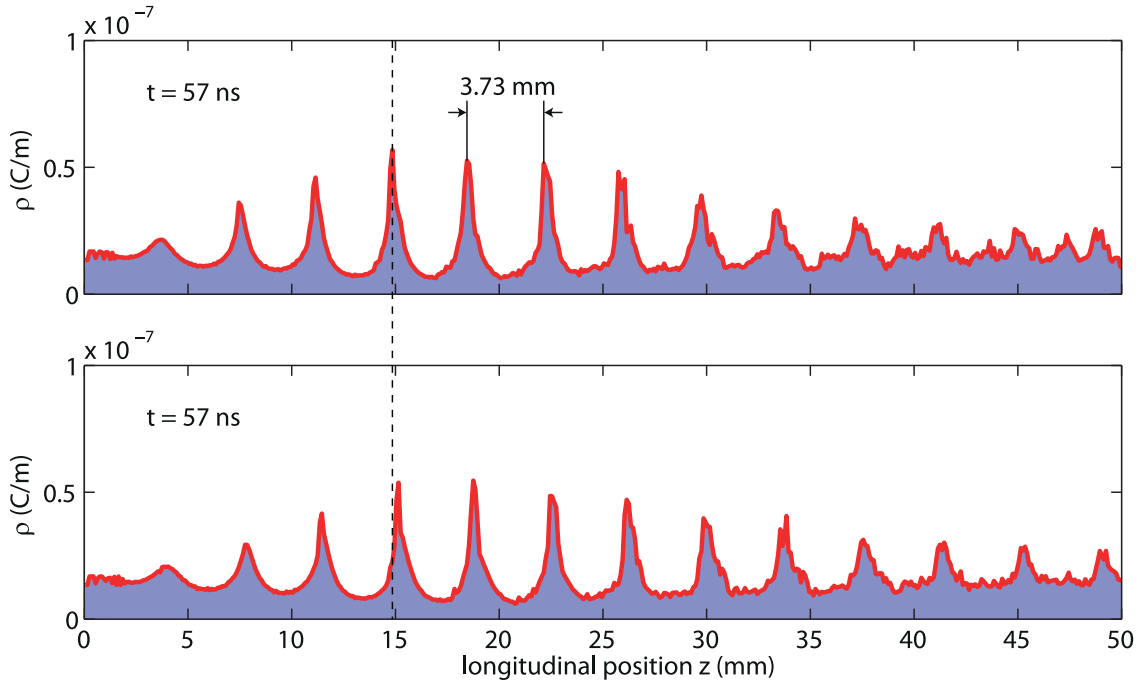

Figure 5.7: *The line charge density in the (top) first electron beam and (bottom) second electron beam at t = 57 ns. The rise times of the beam current is 0.1 ns and 10 ns for beam 1 and beam 2 respectively.*

shows that the phase difference between the two probe signals is about zero just in front of the output port. Figure 5.6 confirms this and actually shows that, at the time t = 57 ns, the phase difference is also zero throughout the whole PhC.

Similar to the study with the field probes, we investigate the effect of a different rise time for the two beams, now using the bunching as a monitor. The field monitors (Figure 5.5(b)) show that once the spectrum has condensed to a single frequency at about 40 ns and a cross-correlation calculation becomes meaningful, a phase difference was detected between the field measured by the two monitors. Figure 5.7 shows the line charge density versus the longitudinal position, again at t = 57 ns. Similar as in Figure 5.6, the top and bottom graph show the charge density for the left beam and the right beam, respectively. Figure 5.7 shows two remarkable features. First, the bunching in the two beams is not identical any more, as illustrated by the fourth bunch in the beam located at z ≈ 15 mm. Second, comparing Figure 5.7 with Figure 5.6 shows that the position of all the bunches have shifted, i.e., the fourth bunch is at z ≈ 15 mm for the beams with different rise times, while they are at z ≈ 16 mm for the beams with equal rise times. Both bunching profiles are measured at the same time of 57 ns after the start of the simulation. For the case with different rise times, the second beam reaches it maximum current at 10 ns, which approximately corresponds to the onset of exponential growth when the structure is pumped by a single beam. When the structure is pumped by two beams having the same rise time, the onset of

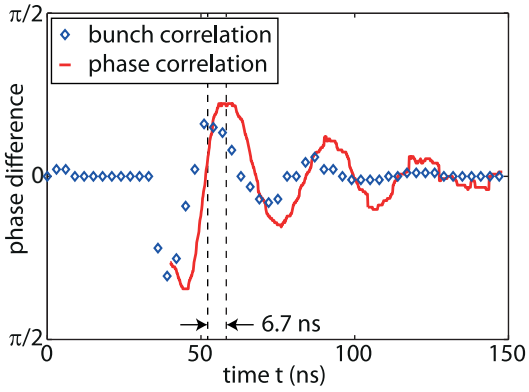

Figure 5.8: *The solid line indicates the phase difference calculated with the cross-correlation between the E_y field as shown in Figure 5.5(b). The diamond markers indicate the phase difference in the bunches in the two separate electron beams. The phase difference in the E_y field clearly follows the phase difference between the electron bunches.*

exponential growth is shifted to about 20 ns. First we can conclude that when two electron beams are present, the laser takes longer to reach the exponential growth regime. A second conclusion is that the longer rise time of the second beam is not sufficient for the first beam to become dominant and set the phase of the radiation field.

To investigate the bunching behavior in more detail a spatial cross-correlation between the line charge density of the left electron beam and the right electron beam is calculated as a function of Δz. The value of Δz can be converted to a phase difference using the wavelengths of the radiation field, i.e., the period of bunching, $\theta = 2\pi\frac{\Delta z}{\lambda}$. Because the line-charge density is calculated using a binning operation on the longitudinal positions of the particles, the resolution is limited by the binning size. Here we used a 10 μm binning size, therefore the resolution in θ is 0.017 rad.

For various times, we have calculated the cross-correlation and determined the phase difference at where a maximum cross-correlation is obtained. This phase difference is plotted as a function of time in Figure 5.8, together with the phase difference obtained in a similar way from the temporal cross-correlation of the two E_y fields monitored at the probes.

The calculated correlations between the bunches in the different electron beams is depicted in Figure 5.8 and compared to the phase correlation of the electric field we observed in Figure 5.5(b). Both correlation traces show a similar oscillation period, while the damping of the oscillation in the phase difference is slightly higher when the phase difference is derived from the bunching. The difference in damping may be explained by the fact that the field probes monitor the E_y field component at a particular transverse position, while in determining the line-charge density the particles are summed over transverse cross-sections. This figure also shows a temporal shift between the results of the two methods. The shift between the two methods can be explained as follows. The line-charge density is calculated at a particular time t_0. The bunching is determined by the phase-matched radiation field, and the interaction is with the backward wave ($v_g < 0, v_{ph} > 0$). This means that the radiation field responsible for this bunching first travels towards the electron

source, is reflected and then travels to the output port. The length of the PhC divided by the group velocity determines the duration Δt of the radiation wave observed at the positions of the field probes. The start of this interval at the position of the field probes is thus $t_0 + \Delta t + \Delta\tau$, where $\Delta\tau$ (~ 0.1 ns) is the time required for the radiation wave to propagate through the output waveguide. As the temporal cross-correlation value is allocated to the center of the interval, a phase difference observed in the spatial cross-correlation at time t_0 should be observed in the temporal cross-correlation at a time $t_0 + \frac{3\Delta t}{2} + \Delta\tau$. From Figure 5.8 we deduce $\frac{3\Delta t}{2} = 6.6$ ns, or $\Delta t = 4.4$ ns. From this, the group velocity is $1.1 \cdot 10^7$ m/s ($= 0.038$c). This value is very close to the group velocity calculated from the band diagram shown in Figure 5.2 at this frequency (15.9 GHz). Note that the window used for the spatial cross-correlation (50 mm $\sim$ 4.4 ns) and the temporal cross-correlation (4 ns) are very similar. Still, the slight difference in window may also be a reason for the observed difference in damping of the phase difference oscillation.

So far, the temporal cross-correlation of two field probe signals gives us information about phase front evolution at only two points in the transverse plane. The spatial cross-correlation of the line-charge density, which sums all electrons in thin electron slides, give remarkable similar results, and therefore suggests that this method can also be used to obtain information about the evolution of the phase front. However, here a transversely integrated measure is obtained. We therefore apply yet another method to investigate the evolution of the phase front and this will be discussed in the next section.

5.5 Direct phase front observation

In the previous sections we discussed methods to obtain information about the phase front evolution in a pFEL. The first method related on measuring the field component as a function of time at two locations in the transverse plane, just before the output port. These field probes can in principle be placed everywhere in the device and measure the total electron field at the probe position. The other method we investigated relied on obtaining the line-charge density in each electron beam. From the evolution of the bunching, information is obtained about the phase front of the radiation field, as the field drives the bunching. Because we use the line-charge density, only information at the location of the electron beams is available.

We therefore investigate yet another method that provides a field map throughout the whole interaction region at a particular time. However, a 3D map would exceed by far the available computational resources and we have to limit ourselves to a 2D map of a single field component. Again, E_y is chosen as the component to register. Even with such measures we can not store many field patterns during the calculations and we limited the number of snap shots to a few. Figure 5.9 shows the E_y field at the xz-plane at y = 0 of the calculation domain for the case that the two electron beams have both a rise time of 0.1 ns. The circles indicate the position of the posts. In the output waveguide, zero crossings of the E_y field are indicated with the black crosses. The electric field inside the PhC, hence inside the resonator, is much larger than the electric field value inside the output waveguide, due to the reflection at the interface between the PhC and the output

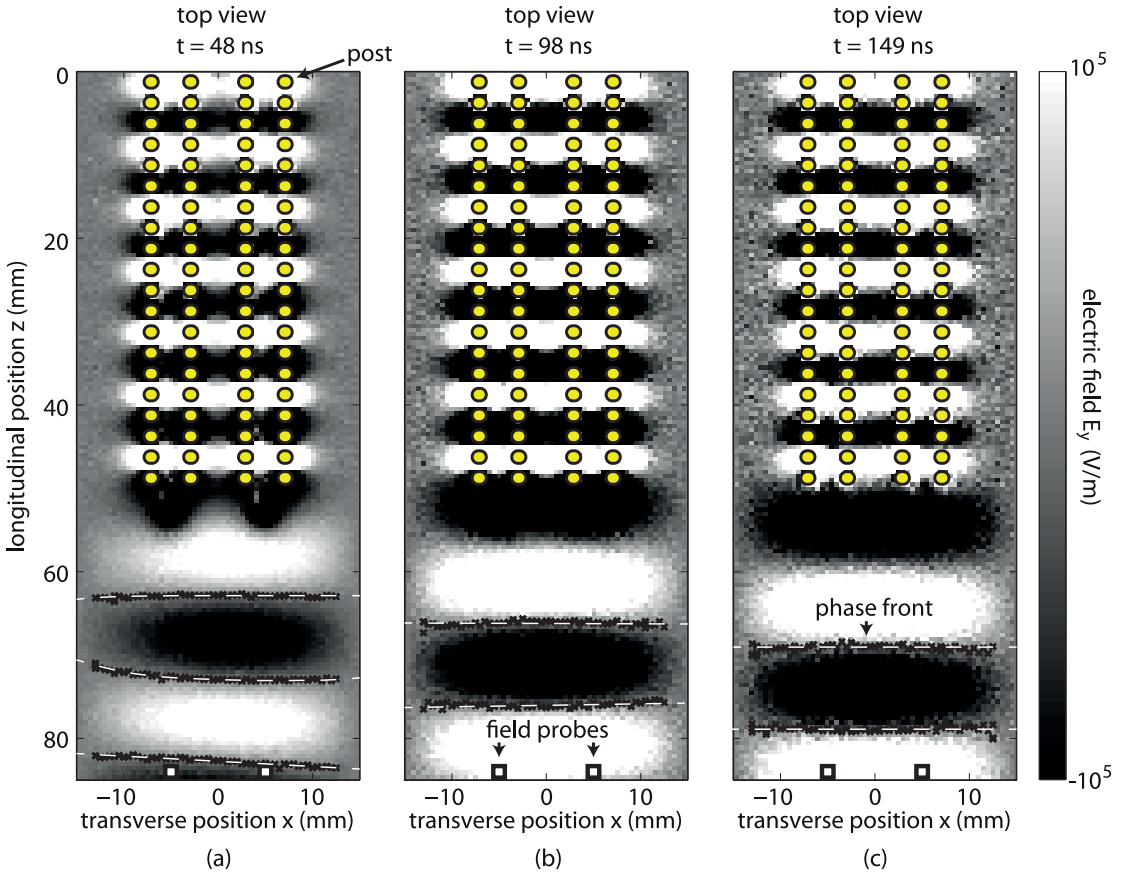

Figure 5.9: *E_y field for (a) 48 ns, (b) 98 ns and (c) 149 ns. The gray scale indicates the electric field value, which is clamped to a maximum and minimum value of -10^5 and 10^5 respectively. The circles and the two squares indicate the position of the posts and the probes respectively. The black crosses together with the dashed white lines indicate the zero-crossings of the electric field, hence the phase front.*

waveguide. Therefore, the electric field values are clamped to a minimum and maximum of -10^5 V/m and 10^5 V/m, respectively. The gray scale is merely to illustrate the phase front. The black squares at the bottom indicate the position of the probes.

As only a limited number of field maps can be produced, the times chosen for the maps in Figure 5.9 are selected using Figure 5.5 to obtain maps with potentially interesting features. The first map at t = 48 ns corresponds to the largest phase front observed with the field probes. Indeed, a tilted wave front is observed in Figure 5.9(a). However, this tilt is not constant throughout the model. A tilted wavefront in the output waveguide necessarily requires the presence of multiple modes. A priori, the PhC eigenmode at the transition from the PhC to the output waveguide can also be described as a super position of propagating and non-propagating empty waveguide modes. The non-propagating modes decay exponentially and can be ignored after some distance

from the transition plane and only the propagating modes remain. Note that in Figure 5.9(a) some contribution from the electron beam to the E_y field is visible at the location where the electrons are dumped. In Figure 5.9(b) and (c), these contributions are still there, but they are masked by the overlapping .

If the PhC eigenmodes would be the same at all three times and only differ in power, we would expect the same decomposition in empty waveguide modes. However, the three maps in Figure 5.9 seem to indicate that this is not the case. This indicates that the radiation field inside the crystal not only grows in power with time, but also changes in mode content. On the other hand, part of the propagating radiation field in the output waveguide may also come from the bending of the bunched electron beams. Because of the difference in radiation power generated inside the PhC, this contribution may be masked in Figure 5.9(b) and (c), while it is visible in Figure 5.9(a), leading to higher order modes in the output waveguide. This needs to be further investigated.

A similar field map is made for the other case investigated so far, where the right electron beam has a rise time of 10 ns in stead of 0.1 ns. Figure 5.10 shows again three 2D field maps of the E_y component at three times, namely (a) 57 ns, (b) 68 ns and (c) 148 ns, that are now based on features observed in Figure 5.5(b) or Figure 5.8. The features visible in Figure 5.8 are indeed confirmed by the phase fronts observed in Figure 5.10(a)-(c). These and other field maps not shown here, give the impression that the phase front tilt visible in Figures 5.9(a) and 5.10(a),(b) undergo an oscillation as a function of time, as is also visible in Figure 5.8, and are for this reason coined as relaxation oscillation of the phase front tilt.

It should be noted that the output power detected in the fundamental mode at the output port is the same for the two cases studied here. The differences observed in the phase front in the output waveguide section between Figure 5.9 and Figure 5.10 suggest a different higher-order mode content for the two cases. Since we do not believe that this can all be attributed to the bending of the electron beam, we have to conclude that the slower rise time of the right electron beam clearly affects the interaction and coupling between the electron beams. Still, given sufficient time, the electron beams become phase-locked and single mode operation is obtained.

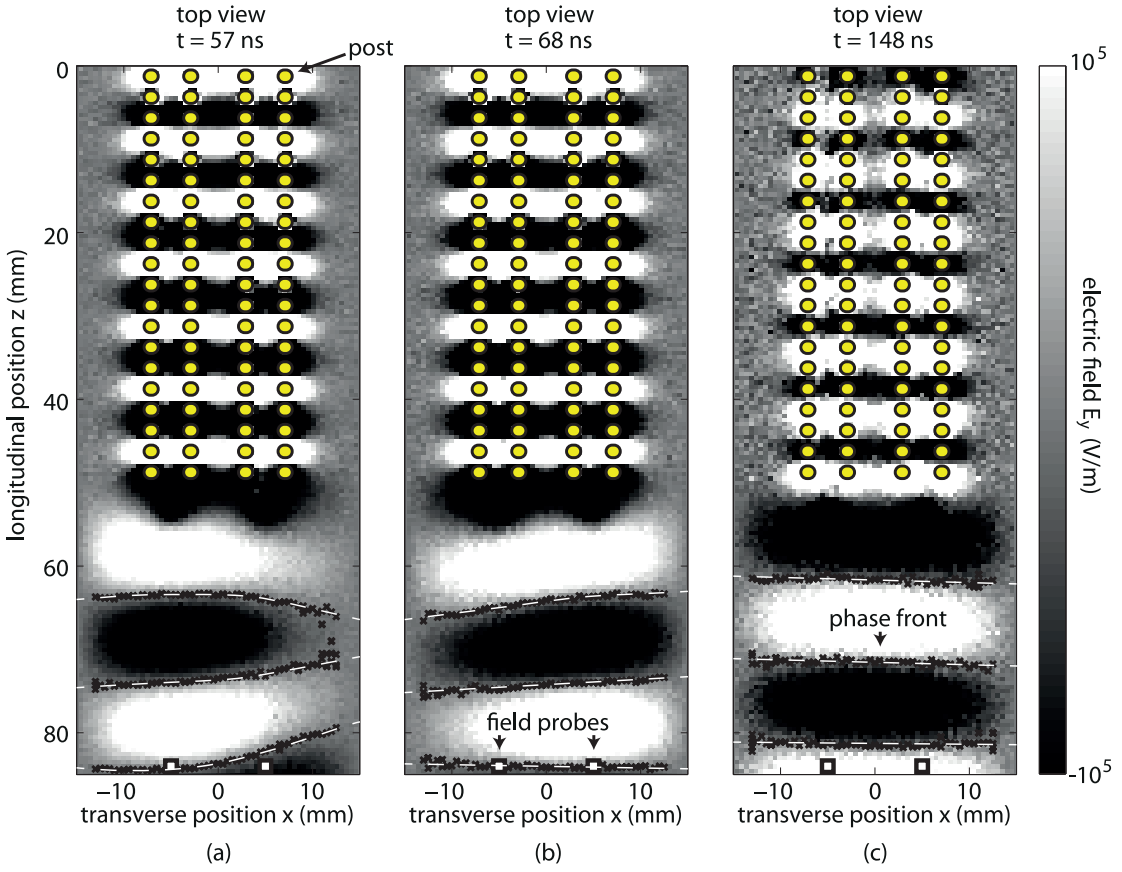

Figure 5.10: *E_y field for (a) 57 ns, (b) 68 ns and (c) 148 ns. The gray scale indicates the electric field value, which is clamped to a maximum and minimum value of -10^5 V/m and 10^5 V/m respectively. The circles and the two squares indicate the position of the posts and the probes respectively. The black crosses together with the dashed white lines indicate the zero-crossings of the electric field, hence the phase front.*

Chapter 6

Conclusions

In the numerical study performed for this thesis we have demonstrated that free-electrons streaming through a photonic crystal can generate wavelength controllable, high power and coherent Cherenkov radiation. This so-called pFEL overcomes the fundamental limitation of PhC lasers in terms of wavelength control, in that principally any desirable wavelength can be generated using an appropriate photonic crystal structure. We theoretically investigate such a pFEL in the microwave range (around 16 GHz). We first used the calculation of the photonic crystal eigenmodes to determine the band diagram of the photonic crystal and used these modes to calculated the Pierce small-signal gain. By doing this for a number of photonic crystals, we determined a gain- and tuning range optimized photonic crystal for use in a pFEL.

The strong-signal dynamics of a pFEL are studied using a PIC method, which give a tremendous insight in the nonlinear dynamics of the pFEL. In contrast, the small-signal calculations are limited to estimating solely expected gain and approximate emission wavelengths. The PIC simulations have shown that such pFEL can actually reach the threshold for coherent laser oscillation. We show that the pFEL is able to generate spectrally narrow band laser output of frequencies around 16 GHz with a bandwidth of at most 20 MHz. We observe an excellent agreement between the tuning predicted by the PIC calculations and the expected frequency tuning derived from the eigenmode calculations for the photonic crystal. An oscillation at distinct longitudinal modes are revealed by the PIC calculations. We predict that the described pFEL can provide an output power of almost 1.5 kW when operated by a single electron beam with a beam energy at around 12.5 keV and a beam current of 1 A.

After verifying that the single beam pFEL works successfully we showed that by adding a second identical electron beam, the steady-state output power can be further increased to almost 3 kW. This opens up the general possibility to increase output power of pFELs without the need for electron beams with higher current densities, simply by using many electron beams in parallel. This is of fundamental importance because increasing the current density in electron beams leads to increasingly complicated beam transport (especially at the low beam energies considered here). However, when pumping a pFEL with many beams, the question arise as to what the spatio-

temporal properties of the output would be. To pave the way to a pFEL using multiple electron beams for a wide control of the output power, we investigate these spatio-temporal properties by studying the phase front dynamics in a pFEL pumped by two electron beams. The various methods used to retrieve the phase front from the PIC calculations are (i) retrieving one field component (E_y) as a function of time for two different positions in the transverse plane, (ii) the line charge-density in each electron beam at a particular time and (iii) a two-dimensional field map of one field component at a particular time. We associate the observed phase difference with a phase front tilt oscillation and found that the relaxation oscillations in the wave front tilt have decayed to zero when a steady state is reached for the output power, even when differences are introduced between the two beams (in particular a different rise time). All methods investigated support the conclusion given above, and at the same time they indicate a complicated start-up dynamics that needs to be investigate further. Still, the observed damping of initial phase differences is promising for extending the number of electron beams.

The same principle of exploiting the control of optical properties provided by a photonic crystal in a pFEL can be applied in any other spectral domain due to the scale invariance of the Maxwell equations. A frequency range with complete lack of powerful, tunable and compact laser sources is the THz range [22]. To upscale the radiation frequency to that range, one simply would have to downscale all dimensions of the PhC. Inevitably, the vacuum channels reduce in size, limiting the volume available for the streaming electrons. In view of the limits in the beam current density, the output power will reduce if only a single beam is used. However, the concept of the pFEL with several or many electron beams, as we have shown here with two beams, can compensate for the power loss by increasing the transverse size of the PhC and the number of electron beams. This should ultimately allow to build hand held, Watt-level continuous wave THz sources.

Bibliography

[1] E. Yablonovitch, "Inhibited spontaneous emission in solid-state physics and electronics," Phys. Rev. Lett. **58**, 2059–2062 (1987).

[2] P. Lodahl, A. F. van Driel, I. S. Nikolaev, A. Irman, K. Overgang, D. Vanmaekelbergh, and W. L. Vos, "Controlling the dynamics of spontaneous emission from quantum dots by photonic crystals," Nature **430**, 654–657 (2004).

[3] M. Fujita, S. Takahashi, Y. Tanaka, T. Asano, and S. Noda, "Simultaneous Inhibition and Redistribution of Spontaneous Light Emission in Photonic Crystals," Sciene **308**, 1296–1298 (2005).

[4] A. Rodenas, G. Zhou, D. Jaque, and M. Gu, "Rare-earth spontaneous emission control in three-dimensional Lithium Niobate photonic crystals," Adv. Mater. **21**, 3526–3530 (2009).

[5] M. R. Jorgensen, J. W. Galusha, and M. H. Bart, "Strongly modified spontaneous emission rates in Diamond-structured photonic crystals," Phys. Rev. Lett. **107**, 143 902 (2011).

[6] M. D. Leistikow, A. P. Mosk, E. Yeganegi, S. R. Huisman, A. Lagendijk, and W. L. Vos, "Inhibited Spontaneous Emission of Quantum Dots Observed in a 3D Photonic Band Gap," Phys. Rev. Lett. **107**, 193 903 (2011).

[7] H. Altug, D. Englund, and J. Vuckovic, "Ultrafast photonic crystal nanocavity laser," Nature Phys. **2**, 484–488 (2006).

[8] R. Colombelli, K. Srinivasan, M. Troccoli, O. Painter, C. F. Gmachl, D. M. Tennant, A. M. Sergent, D. L. Sivco, A. Y. Cho, and F. Capasso, "Quantum cascade surface-emitting photonic crystal laser," Science **302**, 1374–1377 (2003).

[9] C. Cohen-Tannoudji, B. Diu, and F. Laloe, *Quantum Mechanics (2 vol. set)* (WILEY, 1992).

[10] J. M. J. Madey, "Stimulated emission of bremsstrahlung in a periodic magnetic field," J. Appl. Phys. **42**, 1906–1913 (1971).

[11] A. Gover and P. Sprangle, "A Unified Theory of Magnetic Bremsstrahlung, Electrostatic Bremsstrahlung, Compton-Raman Scattering, and Cerenkov-Smith Purcell Free-Electron Lasers," IEEE. J. Quantum Electron. **QE-17**, 1196–1215 (1981).

[12] B. W. J. McNeil and N. R. Thompson, "X-ray free-electron lasers," Nature Phot. **4**, 814–821 (2010).

[13] P. T. Farnsworth, "Cathode Ray Tube," (1960).

[14] R. Kompfner, "The traveling-wave tube as amplifer at microwaves," Proc. IRE **35**, 124–124 (1947).

[15] J. R. Pierce, "Theory of the Beam-Type Traveling-Wave Tube," Proceedings of the IRE **35**, 111–123 (1947).

[16] R. Kompfner and N. T. Williams, "Backward-wave tubes," Proc. IRE **41**, 1602–1611 (1953).

[17] H. R. Johnson, "Backward-Wave Oscillators," Proc. IRE **43**, 684–697 (1955).

[18] F. S. Rusin and G. D. Bogomolov, "The orotron, an electronic device with an open resonator and a reflecting grating," Radiophysics and Quantum Electronics **11**, 430–433 (1968).

[19] K. L. Felch, K. O. Busby, R. W. Layman, D. Kapilow, and J. E. Walsh, "Cerenkov radiation in dielectric lined-waveguides," Appl. Phys. Lett. **38**, 601 (1981).

[20] E. P. Garate and J. E. Walsh, "The Cerenkov maser at millimeter wavelengths," IEEE T. Plasma Sci. **PS-13**, 524–530 (1985).

[21] E. Jerby, "Traveling-wave free-electron laser," Phys. Rev. A **44**, 703–715 (1991).

[22] J. H. Booske, "Plasma physics and related challenges of millimeter-wave-to-terahertz and high power microwave generation," Phys. of Plasma **15**, 055 502 (2008).

[23] J. H. Booske, R. J. Dobbs, C. D. Joye, C. L. Kory, G. R. Neil, G.-S. Park, J. Park, and R. J. Temkin, "Vacuum Electronic High Power Terahertz Sources," IEEE Trans. on Terahertz Science and Technology **1**, 54–75 (2011).

[24] C. Paolini, M. Mineo, and A. di Carlo, "Vacuum Electron Tubes for THz Applications," in *URSI GASS* (2011).

[25] C. Luo, M. Ibanescu, S. G. Johnson, and J. D. Joannopoulos, "Cerenkov Radiation in Photonic Crystals," Science **299**, 368–371 (2003).

[26] G. Adamo, K. F. MacDonald, Y. H. Fu, C.-M. Wang, D. P. Tsai, F. J. G. de Abajo, and N. I. Zheludev, "Light Well: ATunable Free-Electron Light Source on a Chip," Phys. Rev. Lett. **103**, 113 901 (2009).

[27] V. G. Baryshevsky and A. A. Gurinovich, "Spontaneous and induced parametric and Smith-Purcell radiation from electrons moving in a photonic crystal built from the metallic threads," Nucl. Instrum. Methods Phys. Res. A **252**, 92–101 (2006).

[28] A. Einstein, "Zur Elektrodynamik bewegter Körper," Annalen der Physik **17**, 891 (1905).

[29] T. A. Moore, *A travelers guide to spacetime* (McGraw-Hill, 1995).

[30] E. Hecht, *Optics* (Addison Wesley, 2002).

[31] J. Jelly, *Cerenkov radiation and its applications* (Pergammon, 1958).

[32] P. Cerenkov, "Visible radiation produced by electrons moving in a medium with velocities exceeding that of light," Phys. Rev. **52**, 378–379 (1937).

[33] I. Frank and I. Tamm, "Coherent Visible Radiation of Fast Electrons Passing Through Matter," Dokl. Aka. Nauk SSSR **14**, 109–114 (1937).

[34] J. L. Lovvorn, "Reactor power monitor utilizing Cerenkov radiation," Joint nuclear instrumentation symposium (1961).

[35] J. D. Joannopoulos, S. G. Johnson, J. N. Winn, and R. D. Meade, *Photonic Crystals Molding the flow of light* (Princeton University Press, 2008).

[36] W. H. Press and S. A. Teukolsky, *A travelers guide to spacetime* (Cambridge University Press, 1986).

[37] A. F. Oskooi, D. Roundy, M. Ibanescu, P. Bermel, J. D. Joannopoulos, and S. G. Johnson, "MEEP: A flexible free-software package for electromagnetic simulations by the FDTD method," Computer Physics Communications **181**, 687–702 (2010).

[38] S. G. Johnson and J. D. Joannopoulos, "Block-iterative frequency-domain methods for Maxwell's equations in a planewave basis," Opt. Express **8**, 173–190 (2001).

[39] N. W. Ashcroft and N. D. Mermin, *Solid state physics* (Holt, Rinehard & Winston, 1976).

[40] H. Ibach and H. Lüth, *Solid-State Physics* (Springer, 2003).

[41] P. C. Clemmow and J. P. Dougherty, *Electrodynamics of particles and plasmas* (Reading, 1969).

[42] A. S. Gilmour, Jr., *Principles of traveling wave tubes* (Artech, 1994).

[43] A. Piel, *Plasma Physics* (Springer, 2010).

[44] C. K. Birdsall and A. B. Langdon, *Plasma Physics via Computer Simulation* (Adam Hilger Book Company, 1991).

[45] M. Mineo and C. Paolini, "Corrugated Rectangular Waveguide Tunable Backward Wave Oscillator for Terahertz Applications," IEEE Transactions on Electron Devices **57**, 1481–1484 (2010).

[46] CST Microwave Studio, www.cst.com.